UC Santa Barbara
UC Santa Barbara Electronic Theses and Dissertations

Title
Impurity Reduction Strategies for III-N Materials Grown by Plasma-Assisted Molecular Beam Epitaxy

Permalink
https://escholarship.org/uc/item/1bg4n44r

Author
Jorgensen, Kelsey

Publication Date
2020

Peer reviewed|Thesis/dissertation

eScholarship.org Powered by the California Digital Library
University of California

UNIVERSITY OF CALIFORNIA

Santa Barbara

Impurity Reduction Strategies for III-N Materials Grown by Plasma-Assisted Molecular Beam Epitaxy

A dissertation submitted in partial satisfaction of the

requirements for the degree Doctor of Philosophy

in Materials

by

Kelsey F. Jorgensen

Committee in charge:

Professor James S. Speck, Chair

Professor Umesh K. Mishra

Professor Claude Weisbuch

Professor Steven P. DenBaars

September 2020

The dissertation of Kelsey F. Jorgensen is approved.

Professor Umesh K. Mishra

Professor Claude Weisbuch

Professor Steven P. DenBaars

James S. Speck, Committee Chair

September 2020

Impurity Reduction Strategies for III-N Materials Grown by Plasma-Assisted Molecular Beam Epitaxy

Copyright © 2020

by

Kelsey F. Jorgensen

Acknowledgements

First, I would like to thank my advisor Jim Speck for guiding me through this process and providing an excellent example of scientific thinking. His assistance with designing experiments, interpreting data, and navigating the world of research has been invaluable to my development as a critical thinker. I would also like to thank my other committee members, Dr. Umesh Mishra, Dr. Steven DenBaars, and Dr. Claude Weisbuch for challenging me to think more fully about my research project and providing useful suggestions during our yearly meetings.

This experience was greatly improved by my fellow Speck group members and members of the UCSB MBE lab. I was fortunate to receive mentorship from past group members Dr. Erin Young, Dr. Elaheh Ahmadi, Dr. Micha Fireman, and Dr. Yuewei Zhang. I want to thank current and former nitride MBE members Jianfeng Wang, Clayton Qwah, Morteza Monavarian, Zach Biegler, Christian Wurm, Richard Cramer, and Christian Robertson for making the lab an intellectually stimulating and fun place to work. I have come to realize that the UCSB MBE lab is a very special place and I feel very lucky to have called it my research home for these past years. Not only was the assistance of lab managers Kurt Olsson and John English crucial for this work to take place, but their patient teaching and friendly chats have made my life much easier as I navigated this process.

I was very lucky to work with highly skilled collaborators in my time at UCSB. Not only was I lucky to benefit from Dr. Bastien Bonef's atom probe tomography analysis, but I am also grateful to him for his help as a co-author of my publications. Dr. Tom Mates assistance with the many SIMS analyses in this work was critical to my experiments and I am immensely grateful for his dedication to obtaining high-quality measurements as well as his

patient and kind instruction on the workings of SIMS. The staff of the Microscopy, XRD, and AFM labs, as well as the Nanofab and Materials office are all excellent and have made my time at UCSB more enjoyable.

Beyond UCSB I would like to thank my friends for their ability to help me remember that there is a world outside of school. I want to thank my family for their love and support throughout this process, especially my parents Lee and Michelle Jorgensen. Their encouragement of my education is a large part of my desire to pursue a PhD. And last and most importantly, I want to thank my husband Aaron Fast for agreeing to move across the country with me and supporting me in more ways than I can count while I pursued this degree.

CV of Kelsey F. Jorgensen

September 2020

EDUCATION

University of California, Santa Barbara

Ph.D. in Materials, expected September 2020

Committee: James S. Speck (advisor), Umesh Mishra, Claude Weisbuch, Steven DenBaars

Northwestern University, Evanston, IL

BS in Materials Science and Engineering, *magna cum laude*, 2015

TECHNICAL SKILLS

Lab: vacuum systems maintenance and troubleshooting, probe station setup

Materials characterization: XRD, SIMS, AFM, SEM

Electrical characterization: capacitance-voltage profiling, Hall effect measurement

Semiconductor processing: photolithography, dry etch techniques, dielectric deposition

Data processing & analysis: Microsoft Excel, MATLAB, Origin

EXPERIENCE

University of California, Santa Barbara, CA

Graduate Student Researcher, Materials Department, September 2015 – present

- Developed expertise in metal-modulated growth of III-N materials via plasma-assisted molecular beam epitaxy (PAMBE)
- Developed growth of InGaN alloys at growth rates higher than reported in literature, paving the way for future development of efficient MBE LEDs
- Grew pn diodes designed for high reverse breakdown and low leakage
- Analyzed material quality by investigating impurities via SIMS, CV-profiling, and Hall measurements
- Trained junior graduate students in growth and characterization of III-Ns

Graduate Teaching Assistant, Materials 100A with Prof. Ram Seshadri, Fall 2015

- Collaborated with other TAs to create problem sets to assess class learning and teach new topics
- Led weekly recitation to reinforce class material and expand on class topics

3M Corporate Research Analytical Lab, St. Paul, MN

Summer Intern, Summer 2014

- Created 3D models of products using X-ray microtomography for R&D and marketing applications

- Extended lab image processing capabilities with Avizo Fire and MATLAB software by learning the Tcl language

Northwestern University, Evanston, IL

Undergraduate Researcher, Mason Electroceramics Group, 2012-2015

- Conducted research on the binary join of the transparent conducting oxides (TCOs) GITO and ZITO
- Analyzed samples with diffuse reflectance, X-ray diffraction, conductivity, and thermopower measurements to develop new TCO
- Recognized as a finalist for the Fletcher prize for outstanding summer project

PATENTS, PRESENTATIONS, & PUBLICATIONS

In-Situ Methods of Preventing Interfacial Impurities and Dry Etch-Induced Damage in Regrown III-Nitride Structures. **Kelsey Jorgensen**, Morteza Monavarian, James S. Speck, Patent pending. Application serial no. 62/926,300. October 2019

$In_xGa_{1-x}N$ Alloys Grown by Plasma-Assisted Molecular Beam Epitaxy (PAMBE) with Growth Rates Up to 1.3 μm/hr, **K.F. Jorgensen**, B. Bonef, J.S. Speck, Compound Semiconductor Week 2019 presentation. May 2019

High nitrogen flux plasma-assisted molecular beam epitaxy growth of $In_xGa_{1-x}N$ films, **K.F. Jorgensen**, B. Bonef, J.S. Speck, *Journal of Crystal Growth,* 546 (2020) 125738.

Abstract

Impurity Reduction Strategies for III-N Materials Grown by Plasma-Assisted Molecular Beam Epitaxy

By

Kelsey F. Jorgensen

III-N devices have become critical in the fields of energy-efficient lighting and power electronics. Though III-N devices have different materials requirements depending on the end application of the device, one thing common to all devices is the need for extremely pure films. Impurities originating from the atmosphere, wafer processing, or source materials are detrimental both to optoelectronic and transistor devices. This work investigates several impurities found in III-N films grown by plasma assisted molecular beam epitaxy (PAMBE) and analyzes attempts to prevent their incorporation into films.

First Ca was investigated as a potential impurity in PAMBE films following its discovery as a potent impurity in NH_3-Assisted MBE materials, especially the critical InGaN active region in light-emitting diodes (LEDs). Although measured Ca levels in PAMBE films was found to be much lower than in NH_3-Assisted MBE films, it is still potentially high enough to create a nonradiative recombination center in optoelectronics via Shockley-Read-Hall (SRH) or trap-assisted Auger (TAAR) mechanisms. Growth temperature, the presence or absence of a Ga-adlayer, and Ga-polishing had little effect on Ca incorporation in Ga-polar films. Growth temperature did have a moderate effect on Ca-incorporation into N-polar

films, providing a potential path forward for sequestering Ca in lower layers of future devices away from critical device areas.

Next, impurity incorporation in devices requiring a regrowth was examined with an emphasis on Si which is difficult to remove using cleaning procedures employed in MBE growth. The potential for H-radicals to remove Si from a heated wafer surface prior to a regrowth is examined. Though no Si was removed via the procedure used in this work, there exists the possibility that a higher flux of H-radicals, or possibly the use of O-radicals could still be effective in achieving this goal. InN was used as a sacrificial capping layer on GaN films prior to removal from the growth chamber to protect the critical regrowth interface from being exposed to Si and other impurities. This InN cap was not successful at preventing Si from accumulating on the GaN interface, but could be promising as a sacrificial layer to protect the device from processing-related damage prior to regrowth.

Finally, the growth of InGaN films via PAMBE was explored through the use of a modern, high-flux N plasma unit. This plasma unit has been shown to grow smooth GaN films at growth rates over 7 µm/hr. Using this plasma unit capable of over an order of magnitude higher nitrogen flux than previously available led to the growth of InGaN films at a maximum growth rate of 1.3 µm/hr, which is faster than previously recorded in the literature. This enabled more In incorporation into films at higher temperatures due to the stabilization In-N bonds. An $In_xGa_{1-x}N$ film with $x = 0.05$ was grown at 700 °C, which is the highest growth temperature reported for InGaN in the literature. Increasing the growth temperature range and growth rate of InGaN films is likely to lead to smoother films as well as less impurity incorporation which could finally lead to efficient InGaN-based LEDs grown by PAMBE.

Table of Contents

Chapter 1: Introduction 1

1.1 III-N Overview 1

1.2 III-N PAMBE growth basics 3

1.3 Role of extrinsic point defects in III-N devices 10

1.3.1 Impurities in optoelectronic devices 12

1.3.2 Impurities in transistor deices 16

Chapter 2: Calcium Impurity in PAMBE III-N Material 19

2.1 Introduction 19

2.2 Experimental 24

2.3 Results 27

Growth temperature, wet vs dry growth, and substrate orientation 27

Ga-polishing 33

2.4 Conclusions 34

Growth temperature, wet vs dry growth, and substrate orientation 34

Ga-polishing 36

Chapter 3: Strategies for reducing impurities in regrown PAMBE devices 37

3.1 Introduction 37

3.2 Experimental 46

3.2.1 H-radical cleaning 49

3.2.2 InN capping 50

3.3 Results 52

3.3.1 H-radical cleaning 52

3.3.2 InN capping 54

3.4 Conclusions 56

Chapter 4: Improving impurity incorporation in InGaN by using high N* fluxes 58

4.1 Introduction 58

4.2 Experimental 61

4.3 Results 68

4.3.1 Series 1 68

4.3.2 Series 2 72

4.4 Discussion 76

4.5 Conclusions 81

References 83

Appendix A: Calibration of an optical pyrometer 86

Appendix B: MATLAB code for determination of $In_xGa_{1-x}N$ composition 89

Chapter 1: Introduction

1.1 III-N Overview

The III-N material system is a unique group of materials that combines elements Al, Ga, and In from group III of the periodic table with the group V element N to make AlN, GaN, InN, and alloys of these compounds including AlGaN, InGaN, InAlN, and AlInGaN. III-N compounds are semiconductors that have a bandgap ranging from the deep ultra-violet (6 eV) for AlN [1] to the long infrared (0.67 eV) for InN [2]. Figure 1 shows the bandgap energy of the III-N materials system as a function of lattice parameter compared to other compound semiconductors. These bandgap of these materials spans the entire visible spectrum, making them extremely useful in a variety of applications.

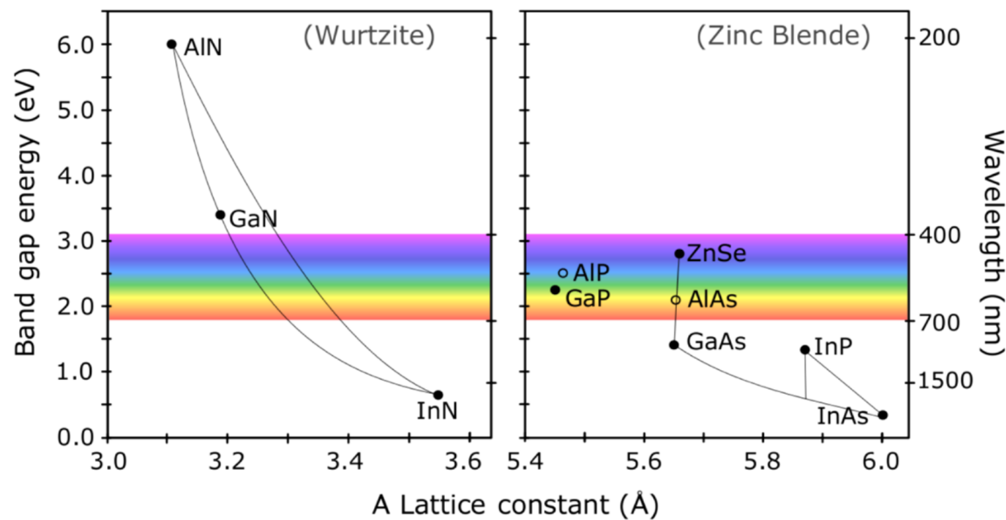

Figure 1. Map of bandgap (E_g) and lattice constant for III-N materials and other semiconductors from Ref [3].

Unlike other III-V semiconductor materials shown in the right plot in Figure 1, III-N materials do not have a cubic zinc blende crystal structure due to the more extreme polarity of the bonds. At room temperature III-N materials have a hexagonal wurtzite crystal structure

shown in Figure 2. These materials have spontaneous electric polarization along the c-axis of the crystal due to the axial point group 6mm of the wurtzite structure. Stressing the III-N materials may lead to additional piezoelectric polarization. Most III-N devices are grown in either the +*c* ("Ga-polar") or -*c* ("N-polar") orientation. In addition to spanning a wide range of bandgap energies, the III-N system also spans a wide range of lattice constants. This causes growth challenges stemming from the lattice mismatch between films of different compositions, which often relax through the formation of defects that deteriorate the quality of the film.

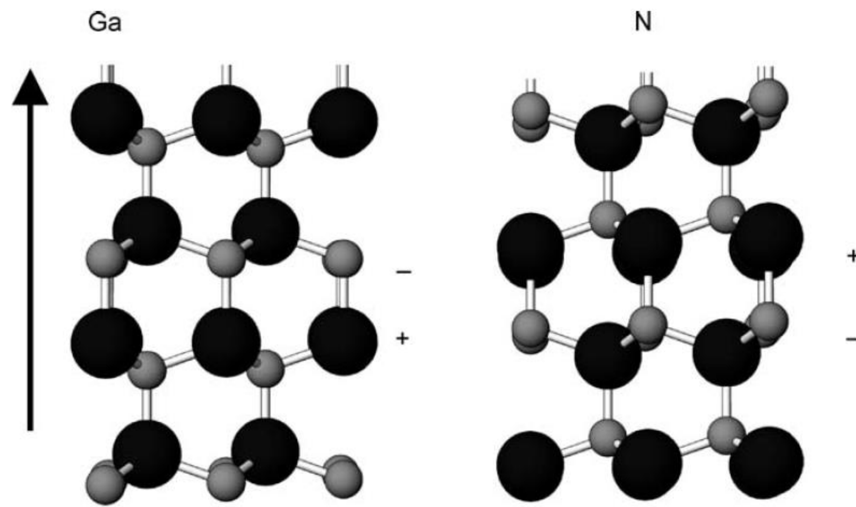

Figure 2. Wurtzite crystal structure of GaN, showing the Ga-polar (left) and N-polar (right) orientations from Ref. [4]. The arrow indicates the +c [0001] direction.

Alloying GaN and InN to make $In_xGa_{1-x}N$ results in a material with a bandgap in the visible spectrum, making this material ideal for visible optoelectronics. Prior to the development of high quality epitaxial III-N materials traditional III-V semiconductors could not be used to produce blue optoelectronics. Due to the work of Shuji Nakamura, Isamu Akasaki, Hiroshi Amano and others efficient blue optoelectronics including light-emitting diodes (LEDs) and lasers. were realized. Blue LEDs revolutionized the field of lighting, due to the ability to

combine blue LEDs with a yellow emitting phosphor to create a white light source. these white LED bulbs are more energy efficient than previous generations of bulbs [5].

The working principle behind a visible LED is to grow an active region made of $In_xGa_{1-x}N$ at a composition x that corresponds to a bandgap at the energy level of the color of desired color of light. This active region is sandwiched between layers with a higher bandgap, usually GaN. This confines electrons and holes in the active region of the device. To produce light, an electron in the conduction band of the $In_xGa_{1-x}N$ combines with a hole in the valence band of the $In_xGa_{1-x}N$, and photon is emitted with a wavelength corresponding to the bandgap.

Though almost all III-N devices are grown by Metal Organic Chemical Vapor Deposition (MOCVD) due to its cost-effectiveness, the growth technique employed in this work is Molecular Beam Epitaxy (MBE). Using the MBE growth technique for III-N growth has several advantages over MOCVD, including active as-grown p-type GaN, historically more abrupt epitaxial interfaces, and lower background impurity content for several species due to the vacuum environment.

1.2 III-N PAMBE growth basics

Molecular beam epitaxy (MBE) is a thin film growth technique that has been in use since the late 1960s to the early 1970s [6]. While most of the early development of the technique focused on GaAs and other, more traditional III-V materials, it has since been used to grow many different materials, including III-Ns. Regardless of the material being grown, MBE systems generally consist of three connected stainless-steel vacuum chambers capable of reaching ultra-high vacuum (UHV). The largest of these chambers is known as the growth chamber and is typically held at the lowest pressure. Precursor materials are typically elemental or in a simple molecular structure to avoid incorporation of unwanted impurities. Elements like Ga, In, Al, Si,

and Mg, are held in pyrolyzed boron nitride or graphite crucibles, and an atomic flux is vaporized or sublimated from the bulk. This flux is carried in a directional beam towards the heated sample surface. Due to the vacuum environment, the mean free path of a particle in the chamber is many orders of magnitude larger than the distance between the crucibles and the sample. This means that atoms or molecules do not interact with one another in the chamber until they reach the sample surface.

Gas precursors such as N_2, NH_3, CBr_4, and many others are commonly used. Gases that can be thermally or chemically decomposed on the sample surface (such as NH_3 and CBr_4) are flowed as-is into the growth chamber. For molecules that have stronger bonds, a plasma can be created to crack the molecules before they reach the sample surface so that the atoms can participate in bonding. N_2 molecules consist of two nitrogen atoms triple bonded together, so it is necessary to create a plasma for N to participate in bonding in III-N crystals. III-N materials can be grown using either NH_3 or an N_2 plasma as a source of nitrogen. Growth by N_2 plasma is known as plasma-assisted molecular beam epitaxy (PAMBE).

III-N growth via PAMBE is a unique method in that it is almost always conducted in a growth regime that is group III-rich. Traditional III-V epitaxial growth wisdom typically dictates that films are grown in a group V-rich environment at a temperature that is high enough to facilitate sufficient adatom mobility on the crystal surface, while not being so hot that the sample is thermally decomposing faster than bonds are being created. The excess group V flux creates an overpressure that prevents bond decomposition in a Le Chatelier-type fashion. However, if GaN growth via PAMBE were grown in this way, the results would be poor. The first electron cyclotron resonance (ECR) and radio frequency (RF) plasma systems used in early PAMBE growth were not capable of providing a sufficient N flux to the sample surface to create more

bonds than were thermally decomposing at temperatures over 850 °C. This made lower growth temperatures necessary. But N-rich growth at these low temperatures results in rough, pitted surface morphology and significant unintentional impurity incorporation. A surfactant was necessary to compensate for the loss of adatom surface mobility that elevated temperatures normally provides. A simple solution was found in the form of a Ga auto-surfactant for GaN growth [7]. At lower growth temperatures during Ga-rich GaN growth a Ga adlayer forms on the surface of the growing film. This liquid-like adlayer enhances surface adatom mobility by providing a channel for enhanced adatom diffusion[8], enabling smooth films with low impurity incorporation. The drawback, however, is that this adlayer must be periodically desorbed to prevent Ga droplet formation on the film surface. Figure 3 shows a schematic of the Ga-adlayer on top of the GaN growth front.

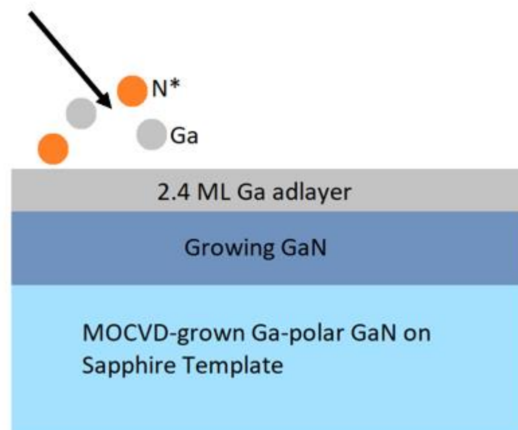

Figure 3. Growth schematic for PAMBE GaN growth in the Ga-polar orientation.

Early studies of the Ga adlayer were conducted by measuring the desorbing Ga-flux (Φ_{Ga}) with a line-of-sight quadrupole mass spectrometer (QMS). These studies revealed that on the Ga-polar (0001) GaN surface, the Ga adlayer coverage is 2.4 monolayers (ML) before the onset of Ga droplet formation[7,9], and 1.1 ML for the N-polar $(000\bar{1})$ GaN surface [7].

GaN grown at 720 °C in Ga-rich conditions under a saturated Ga adlayer produces smooth films with spiral hillock formations typically centered on threading dislocations in the substrate. Figure 4 shows a representative AFM image of a GaN film grown under a saturated Ga adlayer.

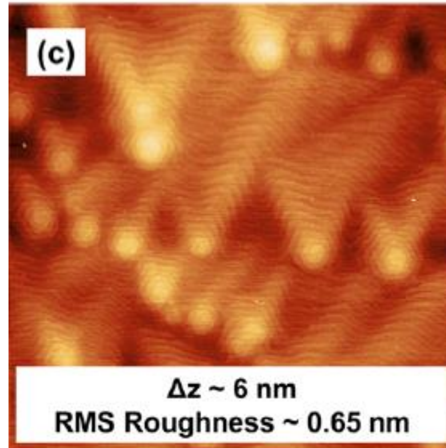

Figure 4. AFM image from Ref. [10] showing the characteristic spiral hillock morphology of GaN grown under a saturated Ga-adlayer.

The exact form of the nitrogen species coming from the RF plasma that participates in III-N growth on the sample surface has been a subject of debate in the literature. Carefully conducted appearance mass spectroscopy (AMS) experiments have indicated that the species that reaches the substrate is atomic N [11], however optical emission spectroscopy (OES) from the back viewport of the plasma has indicated that a meta-stable excited N_2 molecule is also present [12,13] . It is beyond the scope of this work to make a determination about the identity of the active species, and for simplicity the active nitrogen will be represented as N*.

A growth diagram for (0001) GaN showing the various growth regimes is shown in Figure 5. The Ga-rich growth under a saturated Ga adlayer described above is shown on the

figure by the red star. This growth takes place in the intermediate regime very close to the line separating the intermediate regime from the droplet regime.

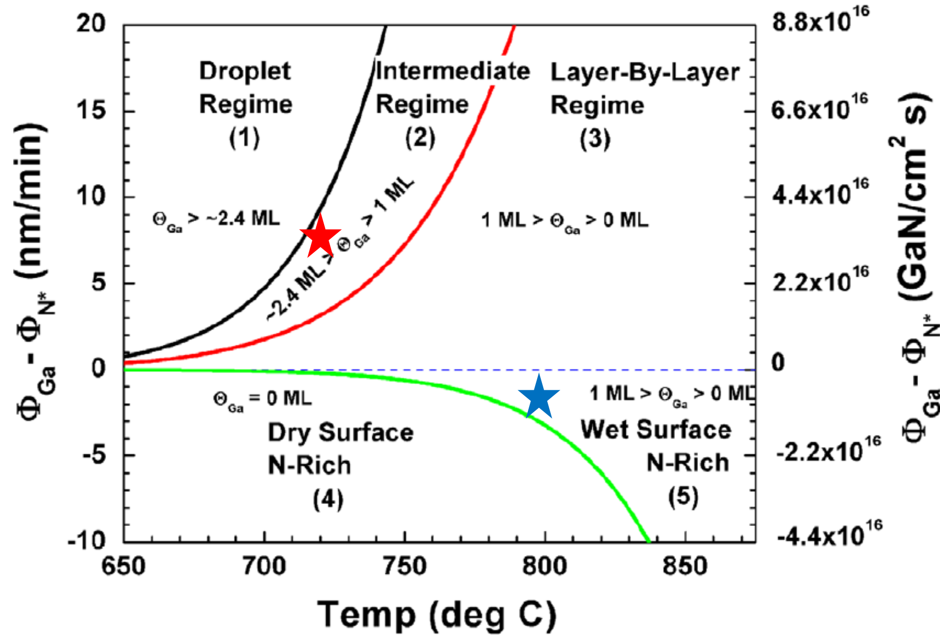

Figure 5. GaN growth diagram from Ref [14].

It is also possible to grow smooth GaN films under high temperature, N-rich conditions indicated by the blue star in Figure 5. With standard N plasma sources this growth is typically slow due to the fact that the Ga-N bonds are actively decomposing in this regime. Ref. [15] achieved an electron mobility 1125 cm^2/Vs for a carrier concentration of 1.1×10^{16} cm^{-3} in this growth regime.

In the experimental sections of this work all samples were grown in a Varian GenII MBE system equipped with effusion cells for Ga (two cells), In, Al, Mg, and Si. Over the course of this research several cells (including one of the Ga as well as the In and Mg) were replaced either to increase the cell capacity or due to a malfunction with an old cell. Two plasma sources are

installed on the system: one Veeco Unibulb RF-plasma unit for standard growth rates, and one modified Riber RFM50/63 RF-plasma unit for higher growth rates. Both plasma sources use N_2 gas of 99.9995% purity. The plasma cavity of the Riber plasma unit was replaced during this research as the original cavity had become damaged from the heat generated by the plasma. The newer cavity resulted in a marked increase in N* flux from the plasma unit, leading to much higher growth rates than the old cavity for the same gas flow rate and plasma forward power.

The MBE system is also equipped with a Staib RHEED gun and a RHEED phosphor screen with camera setup to record the diffraction pattern to enable *in situ* monitoring of the sample surface and metal adlayer. All substrates were coated with 500 nm of Ti on the backside with an electron beam evaporator to ensure good heat distribution to the sample and to provide a source of black body radiation for measurement of the growth temperature via an optical pyrometer. The optical pyrometer was calibrated to the melting point of Al (see Appendix A for the procedure for pyrometer calibration).

Most substrates used in this work are single side polished (SSP) MOCVD-grown (0001) Ga-polar GaN on sapphire from Lumilog St. Gobain with a threading dislocation density (TDD) around 5-8 $\times$ 10^{8} cm^{-2}. Both conducting Si-doped and semi-insulating Fe-doped substrates were used, with [Si] around 3 $\times$ 10^{18} cm^{-3}. Si-doped substrates are known by the supplier's term "STN" and Fe-doped substrates are known by the supplier's term "STINS". Substrates were cleaned prior to loading into the MBE system in a sonicated bath of acetone for 3 min, followed by methanol for 3 min, and finally isopropanol for 3 min. After cleaning, the samples were mounted to a lapped Si wafer with In metal then loaded into the MBE system. Prior to growth samples were outgassed at 400 °C for one hour to remove atmospheric adsorbates from the surface.

Growth of $In_xGa_{1-x}N$ alloys by PAMBE is similar to that of GaN with a few notable differences. The growth temperature of these films is less than 650 °C, and typically in the 500 – 600 °C range [16]. This is due to the instability of In-N bonds at temperatures greater than 435 °C [17]. This means that InGaN growth is taking place while the film is actively decomposing. To overcome the limited adatom mobility at such low growth temperatures, a metal adlayer is employed just as with GaN growth, but instead of a Ga adlayer an In adlayer is used. Figure 6 shows the growth schematic for InGaN films. The saturated In wetting layer rides the surface of growing InGaN film. Using line-of-sight quadrupole mass spectrometry (QMS), the thickness of the saturated In wetting layer on an InGaN film has been determined to be 2.5 monolayers (ML) before the onset of In droplets [17].

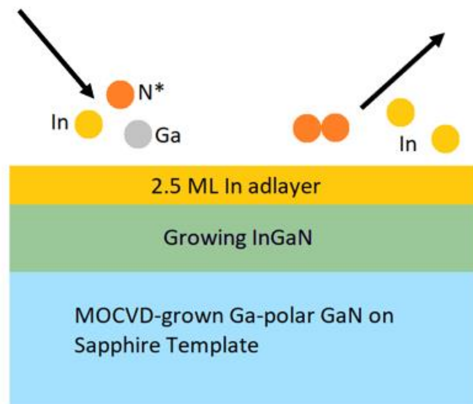

Figure 6. Growth schematic for PAMBE InGaN growth under a saturated In-adlayer.

The overall growth of InGaN is group III rich, but it is imperative that the Ga flux (Φ_{Ga}) is less than the nitrogen flux (Φ_N) to allow In to incorporate into the film. N will preferentially form bonds to Ga atoms before creating thermally unstable In-N bonds. Smooth InGaN film morphologies typically show spiral hillocks around the threading dislocations in the substrate

under atomic force microscopy (AFM) images. Figure 7 shows a representative AFM micrograph of the spiral morphology of an InGaN film.

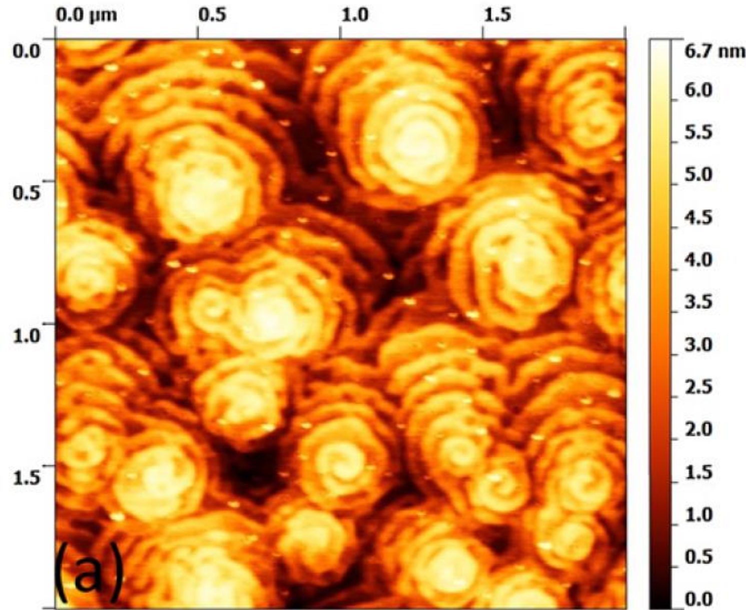

Figure 7. AFM image of InGaN grown in the Group III-rich regime showing spiral hillock formation from Ref. [16].

1.3 Role of extrinsic point defects in III-N devices

Semiconductor technology has always required the utmost atomic purity to take advantage of these materials' natural properties. This work will focus on extrinsic point-defect impurities in III-N materials. Extrinsic point defects are elements present in the material other than those intentionally added during growth. The most common impurities found in semiconductors are those elements which are most abundant on Earth's surface and atmosphere including C, O, H, and Si.

Impurities can come from several sources. On any surface that is exposed to atmosphere there exists a layer of adsorbed of gasses and particles that is attracted by the unsatisfied bonds

present on the surface. Gasses that naturally occur in the environment can be H_2O vapor, CO_2, O_2, N_2, and Ar. Organic material in the form of hydrocarbons are also present, as well as minerals found in soil such as SiO_2, $CaCO_3$, and others. These "atmospheric" impurities collect on the surface of wafers prior to epitaxial growth and incorporate into the crystal during growth. Another source of impurities on the surface of wafers is from the chemical-mechanical polishing that takes place before epitaxial growth to prepare the surface of the wafer.

Impurities can also come from the growth chamber environment while the epitaxial layers are growing. Even though source material used in MBE growth is of the highest purity available (typically seven 9s purity), contamination of the source material can occur during loading into the system. Gas sources can also become contaminated if improper procedures are used when the pressurized tanks are attached to the vacuum system. Other sources of contamination can come from the crucibles used in effusion cells. These crucibles are cleaned by either aqua regia followed by boiling in de-ionized (DI) water for pyrolyzed BN crucibles or by HF followed by a rinse in de-ionized water for graphite crucibles. DI water that is out of specification can cause contamination, as well as the use of dirty tweezers. Finally, impurities in the growth chamber environment can also come from leaks in the vacuum system or gas lines. These chamber-related sources of contamination are relatively rare due to the large knowledge base available to experienced vacuum scientists, however, inexperienced researchers may unintentionally overlook these clean handling procedures.

For devices that require a regrowth, an additional source of impurities can come from processing-related issues. A regrowth refers to when a device is partially grown in the reactor, then removed for external processing including photolithography and etching, then is returned to the growth chamber where the remainder of the device is grown. These photolithography and

etch processes introduce contamination on the surface. High-energy dry etch processes are especially likely to introduce elements that are often implanted in the films and are difficult to remove.

Standard growth processes used in MBE growth help to eliminate some of the impurities associated with the substrate surface. These cleaning methods broadly fall into two categories: *in situ* and *ex situ* cleaning methods. *Ex situ* cleaning refers to cleaning procedures that are applied to substrates before they are loaded into the vacuum system. In this work a standard solvent clean was performed on all samples that consisted of the sample being submerged for 3 minutes each in acetone, then methanol, then isopropanol while in an ultrasonication bath. These solvents are most effective at removing any organic material from the wafer surface. Other *ex situ* cleaning methods include dips in various acids or bases as well as ozone cleans. If the location of the *ex situ* cleaning procedures is different from the location of the MBE system, it is common to use vacuum sealing to protect the wafer surface from collecting more impurities during travel to the MBE system.

In situ cleaning methods refer to processes that take place after the substrate has been loaded into the MBE system. Once the substrates are loaded into the vacuum chamber, they are typically degassed at higher temperature to drive off gaseous contaminants like H_2O and CO_2. In this work all samples were degassed in the buffer chamber of the MBE system at 400 °C for 1 h prior to growth. Other *in situ* cleaning methods used in PAMBE include Ga-polishing and plasma cleaning.

1.3.1 Impurities in optoelectronic devices

Impurities are of the most concern in optoelectronic devices in the active region, the area of the device where electrons and holes recombine to produce photons with an energy equivalent

to the band gap of the material. In most LEDs and lasers that emit in the visible spectrum, the active region is composed of InGaN/GaN multi-quantum wells (MQWs). Alternating layers of InGaN quantum wells (QWs) and GaN (or lower In composition InGaN) quantum barriers (QBs) ensure that electrons and holes are trapped in the potential wells of the InGaN layers and recombine in the InGaN QWs.

In an ideal device, all electrons and holes trapped in the QWs will recombine from the minimum of the conduction band to the maximum of the valence band to produce photons with energy equal to the band gap of the InGaN QWs. In reality however, some of the charge carriers recombine via other mechanisms that do not result in the emission of photons at the desired wavelength. Impurities are the cause of several of these nonradiative recombination mechanisms. When impurities incorporate into a semiconductor, they form additional energy levels in the band structure of the material. When these trap energy levels are in the bandgap of the semiconductor, the impurities can act as nonradiative recombination centers. The two nonradiative recombination mechanisms involving impurities are shown in Figure 8. In Shockley-Read-Hall (SRH) recombination, impurity levels in the band gap cause electrons and holes to recombine from the trap level, resulting in phonon emission instead of from the conduction minimum to the valence band maximum resulting in photon emission. Trap-assisted Auger recombination (TAAR) has recently been shown to be a strong nonradiative recombination mechanism in MBE-grown LEDs [18,19]. In this mechanism electrons and holes recombine at the trap energy and promote another charge carrier to a higher energy level in the crystal.

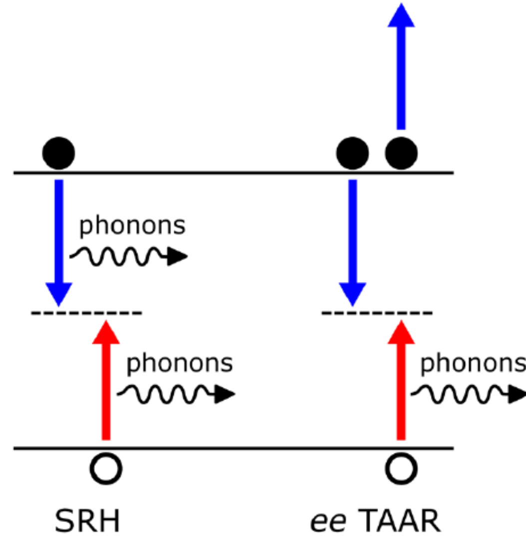

Figure 8. Impurity-related nonradiative recombination mechanisms in optoelectronic devices, Shockley-Read-Hall (SRH) recombination and trap-assisted Auger recombination (TAAR). Adapted from Ref. [18].

While impurities are not the only issue to consider when optimizing the efficiency of III-N LEDs, it is imperative that they be minimized to realize efficient devices. Computational work [20] has shown that even extremely small concentrations (10^{14} cm^{-3}) of impurities can limit the radiative recombination efficiency of optoelectronic devices. Since SRH recombination scales linearly with the carrier concentration, it is often the culprit behind inefficient devices operated at low currents. Since TAAR scales with the square of carrier concentration, it can affect efficiency of devices at moderate to higher currents.

Impurities have also been shown to greatly impact the performance of regrown tunnel junction (TJ) contacts grown on c-plane GaN/InGaN 455 nm LEDs [21]. In these devices, an industry-grown LED wafer was subjected to various pre-growth acid dips followed by vacuum sealing before the NH_3-assisted MBE growth of a n++GaN TJ regrowth. Figure 9 shows that all of the acid treatments resulted in a significant lowering of device voltage as well as a lower turn-

on voltage compared to the reference sample with no pre-growth treatment. HF treatment showed the greatest reduction in voltage (nearly 1.5 V at 20 A/cm^2 compared to the reference device with no treatment). Secondary-ion mass spectroscopy (SIMS) analysis showed that the HF dip removed excess Mg and especially O from the wafer surface prior to regrowth.

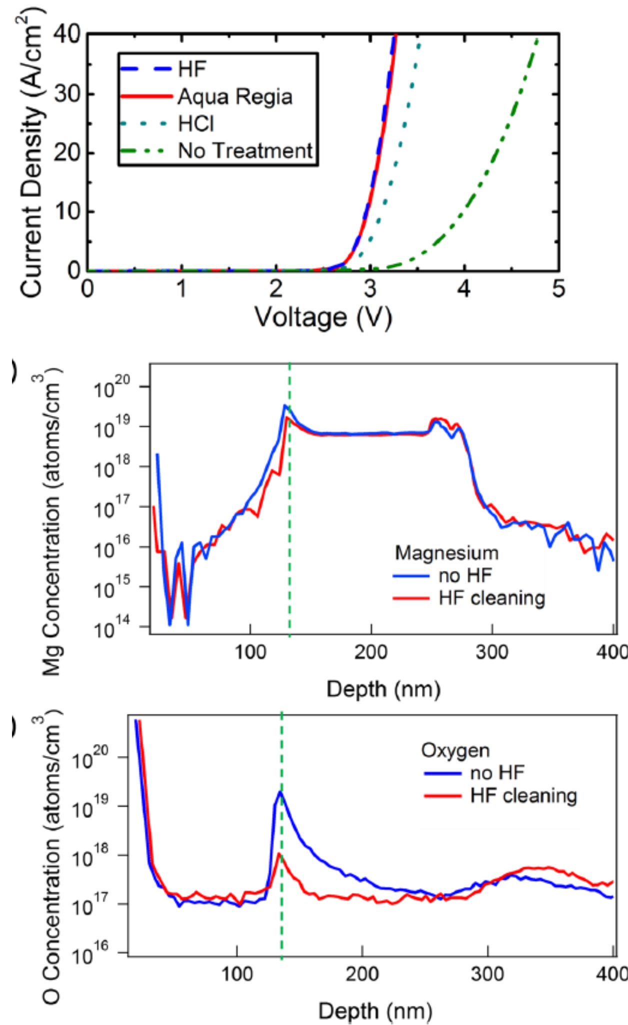

Figure 9. Yonkee *et al* .[21] showed that adding an HF dip before regrowth of a tunnel junction contact on an industry supplied LED wafer reduced the voltage of the device significantly.

1.3.2 Impurities in transistor deices

III-N transistor devices also require extremely low background impurity concentrations to achieve the superior performance for which these wide bandgap semiconductors are known. Of the most common impurities found in nitride films, O and Si are both shallow donors and C is closer to mid-gap. Unintentionally doped nitride films are typically slightly n-type due to the O and Si impurities. Lateral transistor devices require low background impurity concentrations to prevent a parallel conducting channel from interfering with two-dimensional electron gas (2DEG).

For vertical transistor devices, such as the one shown in Figure 10, the background impurity concentration of the n^- GaN drift layer must be as low as possible for these devices to reach the high reverse bias breakdown voltages required. Under reverse bias the device is depleted into the very thick drift region. The reverse bias breakdown voltage is the integral of the electric field which has a maximum at the pn junction interface and reaches a minimum into the drift layer. If the drift region is sufficiently thick (typically several microns), the electric field is triangular, ending at zero for the maximum achievable depletion width $w_{d,max} = \frac{\epsilon F_{br}}{qN_{net}}$, where N_{net} is the net charge in the drift region ($N_{net} = N_D$-N_A). If the maximum depletion width is reached, the integral of the breakdown electric field (which gives the maximum breakdown voltage) is $V_{br,max} = \frac{1}{2} F_{br} w_{d,max} = \frac{1}{2} \frac{\epsilon F_{br}^2}{qN_{net}}$. By minimizing the net charge in the drift region, the reverse bias breakdown voltage can be maximized.

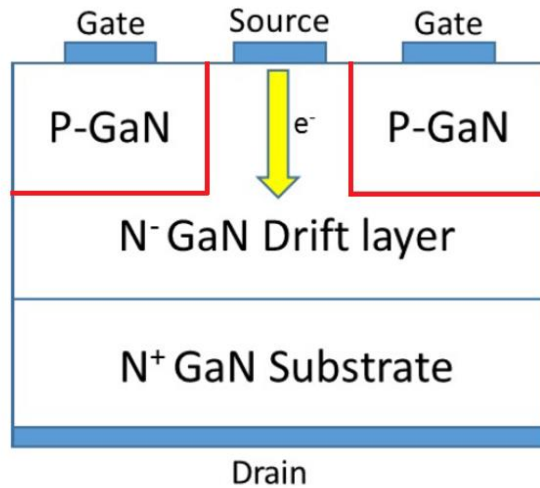

Figure 10. Example of a vertical transistor device from the ARPA-E funding opportunity announcement (FOA)[22]. Regrowth interfaces are highlighted in red.

Figure 11 shows the maximum attainable reverse bias breakdown for various semiconductors as a function of net charge concentration. Nitride devices are typically limited by $N_{net} \sim 10^{15}$ -10^{16} cm^{-3} because they are impossible to grow from the melt like Si, SiC, and Ga_2O_3 which results in lower impurity incorporation. Reported values V_{br} for GaN devices are typically less than 5kV, and often closer to 1 - 2 kV.

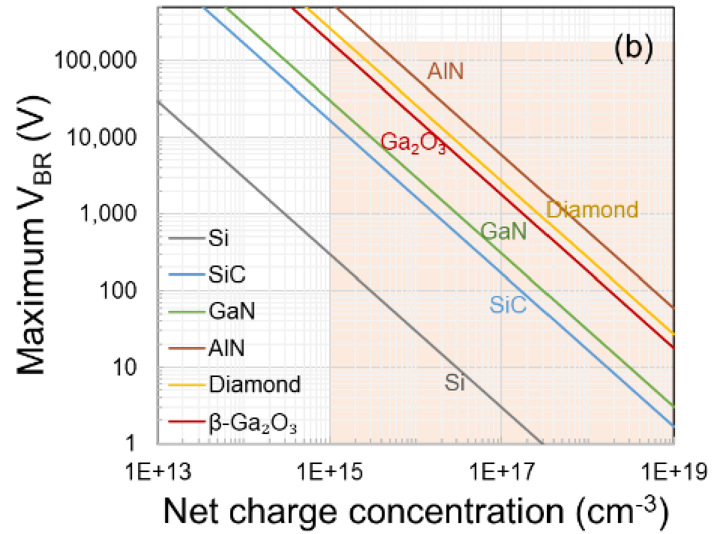

Figure 11. Plot showing the maximum achievable reverse bias breakdown for various semiconductors as a function of net background charge (impurity) concentration[23]. Image courtesy of Dr. Yuewei Zhang.

Chapter 2: Calcium Impurity in PAMBE III-N Material

2.1 Introduction

Although reports of MBE-grown LEDs in the literature suggest that the low efficiency of these devices is likely due to an impurity-related Shockley-Read-Hall center, identification of the impurity (or impurities) has not conclusively been identified. Dr. Erin Young at UCSB identified the presence of calcium in NH_3-MBE grown GaN and InGaN after discussions with Dr. Tom Mates, the lead scientist in secondary-ion mass spectroscopy (SIMS) at the university. The results of this investigation are reported in Ref. [24].

When SIMS was performed on a commercially available LED epitaxial stack, [Ca] levels (along with Cu, Ni, Fe, and Ti) were found to be at or below the detection limit of the SIMS system. However, a NH_3-MBE grown stack consisting of an n-doped GaN layer, 3× InGaN/GaN multi quantum well (MQW) region, and a UID GaN cap showed a spike in [Ca] at the regrowth interface of 7×10^{16} cm^{-3}, 8×10^{15} cm^{-3} in the n-type region, and approximately 10^{18} cm^{-3} in the InGaN QWs (shown in Figure 12). It is important to note in the SIMS data in Figure 12 that after the InGaN multi-quantum well (MQW) region, the [Ca] in the UID GaN cap was 2×10^{15} cm^{-3}, which is lower than it was in the previous n-doped region.

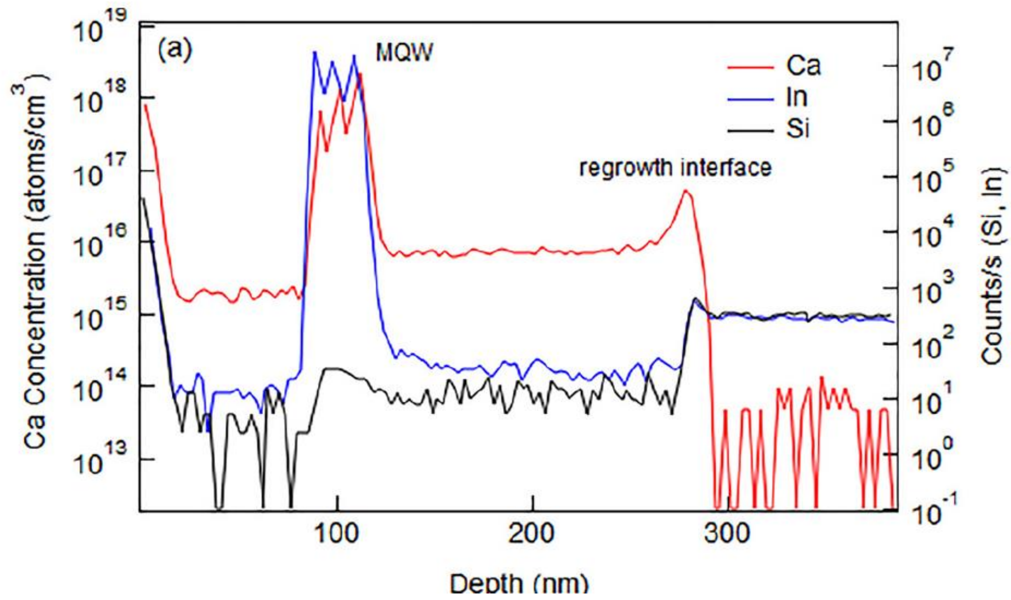

Figure 12. SIMS profile of NH_3-MBE grown epitaxial stack showing the presence of large [Ca] from Ref. [24].

Impurity levels this high (~10^{18} cm^{-3}) in a QW are very likely to be SRH non-radiative recombination centers, so this finding was very promising. If the Ca could be eliminated or greatly reduced in the QWs, vast improvements in internal quantum efficiency (IQE) for MBE devices could be realized. Computational work in Ref. [20] supports the likelihood of Ca on a Ga site being a SRH center in InGaN, with Ca acting as a deep acceptor. Shen et al. [20] found that for [Ca] of 10^{17} cm^{-3} in a green LED, 20% of the carriers could be lost to SRH recombination.

The SIMS data in Ref. [24] suggest that Ca incorporation in the film is temperature-dependent, since the growth temperature for both GaN layers in the sample is 820 °C, and the growth temperature for the InGaN layers is 600 °C. The source of the Ca contamination can also be deduced from the SIMS results. If the Ca were coming from the growth chamber environment, the [Ca] should be the same in the underlying GaN region and top UID GaN layer since they are grown under the same growth conditions. However, since the top region shows a

reduced [Ca], this supports the conclusion that there is a finite amount of Ca at the substrate surface prior to growth, and that capturing it in lower layers of the film can leave upper layers with much less [Ca].

To confirm surface contamination as the source of Ca, Young et al. [24] grew an additional sample that was identical to the first, except with the inclusion of a low-temperature (600 °C) GaN layer in the GaN buffer. SIMS results showed that Ca incorporated in high concentration in the low temperature GaN layer, but was then reduced greatly in the InGaN/GaN MQW region compared to the sample shown in Figure 12 (approximately 10^{15} cm^{-3} instead of the previous ~10^{18} cm^{-3}). This confirmed surface contamination as the source of Ca. Even though epitaxial substrates are handled and cleaned with extreme care to reduce impurities at regrowth interfaces, some impurities will always remain. Based on these findings, a strategy was developed to consume as much Ca as possible in the lower layers of films so that MQW regions above would be free from too much Ca that could be a source of SRH non-radiative recombination centers.

Simply having one thick low temperature (LT) GaN layer in the buffer would result in poor surface morphology that could be impossible to recover once the top layers of a device were grown. To solve this issue a 10 period superlattice (SL) was used with alternating layers of 5 nm LT 600 °C GaN to capture Ca followed by 20 nm of high temperature (HT) 820 °C GaN to recover any roughening caused by the low temperature layer. SIMS analysis of this sample is shown in Figure 13. This superlattice was successful in reducing [Ca] in the layers above the SL below 10^{14} cm^{-3}, which was comparable to the MOCVD-grown substrate. Further modeling was done based on the SIMS results to quantify the initial [Ca] on the substrate surface as well as the magnitude of the surface segregation. Next, simplified LEDs were grown with and without the Ca-reducing SL and the I-V and L-I curves were compared. The LED grown with the SL showed

a 10 times improvement in light output power compared with the reference LED at low injection currents and showed a 2 times improvement in external quantum efficiency (EQE).

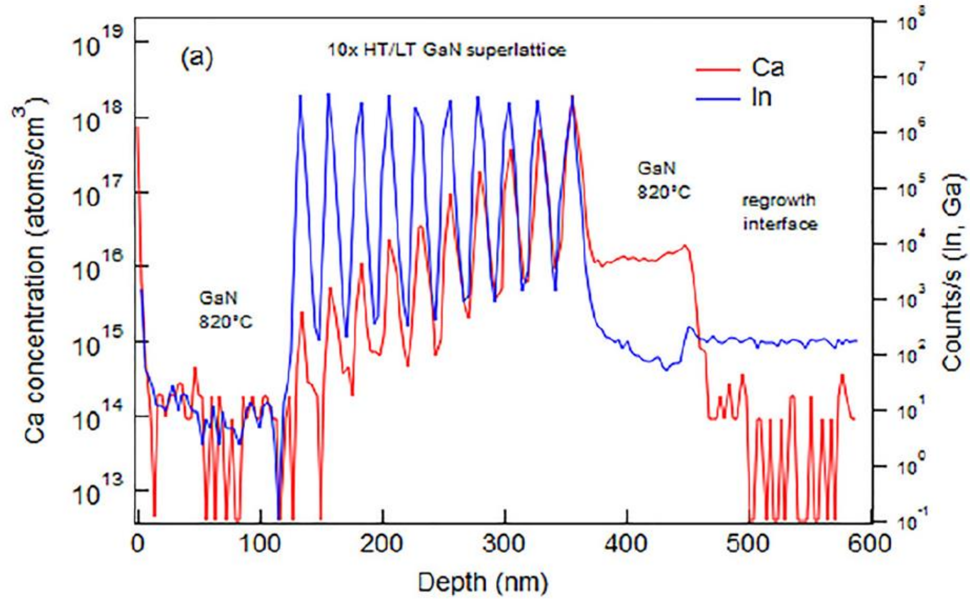

Figure 13. SIMS showing [Ca] in the LT GaN/HT GaN SL from Ref [24]. [Ca] is reduced by several order of magnitude by the SL.

In this study the Ca incorporation was found to be extremely temperature dependent, which may provide the answer as to why MOCVD-grown III-N material does not show these elevated [Ca] issues. MOCVD grown typically takes place at temperatures much higher than both NH_3-MBE and PAMBE (around 1000 °C - 1100 °C for GaN growth). At these higher growth temperatures, Ca likely rides the growth surface instead of incorporating into the film. Sources of Ca contamination on the substrate surface could be due to the chemical mechanical polishing (CMP) of the samples or even de-ionized water. Additionally, Ca has been identified on surfaces of Si and GaAs wafers in prior studies [25,26]. It is also possible that the SL employed by Young et al. [24] could also be reducing the concentration of as yet unidentified impurities.

This study presents an exciting path forward for realizing efficient LEDs grown by NH_3-MBE, but its extension to PAMBE LEDs is also apparent. Since PAMBE growth typically takes place at an even lower growth temperatures than NH_3-MBE, it stands to reason that Ca could be even more of an issue for this growth technique. Optimal GaN growth temperature for Ga-rich PAMBE is around 720 °C, and growth temperatures for InGaN can vary anywhere from 500 °C – 600 °C. In addition to effects from growth temperature, Ca incorporation in PAME material could also depend on whether the growth is Ga-rich or N-rich.

For the investigation into Ca incorporation into PAMBE III-N films, several growth parameters were identified as possible candidates for factors that may influence how much Ca incorporated into the film. Since growth temperature was identified as a strong factor that influenced the incorporation of Ca in Ref. [24], this growth parameter was also investigated in this study. Unlike NH_3-MBE growth, PAMBE growth can take place both under a Ga-adlayer in Ga-rich growth conditions or without a Ga-adlayer under N-rich growth conditions. Since previous literature indicates that impurity incorporation differs greatly for these two growth modes, they were both investigated in this study. Henceforth, growth under a Ga-adlayer in Ga-rich conditions will be referred to as "wet" growth, and growth without a Ga-adlayer under N-rich conditions will be referred to as "dry" growth. Additionally, comparison between Ca incorporation on Ga-polar GaN substrates vs N-polar GaN substrates was also performed.

A strategy to remove Ca from the substrate surface before growth was also studied. Ga-polishing is a well-established technique often employed in PAMBE III-N growth to remove impurities from the surface of a substrate. In this technique, Ga metal is deposited onto the sample surface while the substrate is around growth temperature. This forms a Ga-adlayer. Then the Ga cell is shuttered and the adlayer is thermally desorbed, taking impurities from the sample

surface with it. This cyclical process is repeated several times. This method has been shown to be extremely effective at removing O and C from the sample surface, and has had some success removing Si [27–29].

2.2 Experimental

To first quantify the baseline level of Ca in PAMBE films, two reference structures were grown on Ga-polar substrates. The first reference structure, Reference Sample A, consisted of about 650 nm unintentionally doped (UID) GaN grown on a STN substrate. This sample was grown at 720 °C under a saturated Ga-adlayer in Ga-rich conditions. The second reference structure, Reference Sample B, replicated the reference structure in Ref. [24]. It consisted of 150 nm UID GaN, a 3 QW InGaN/GaN MQW region, and a 75 nm UID GaN cap. The thick GaN layers were grown at 720 °C under a saturated Ga-adlayer in Ga-rich growth conditions. The InGaN QWs were grown at 575 °C under an In-adlayer. The GaN QBs consisted of 30 s of GaN growth under Ga-rich conditions at 575 °C, followed by 1 min of GaN grown under the previously mentioned 720 °C Ga-rich growth condition. The procedure for growth of the GaN QBs was chosen to ensure that the InGaN QWs were capped before the sample was heated back to 720 °C, to prevent the QWs from decomposing. Figure 14 shows a schematic of the structure of Reference Sample B.

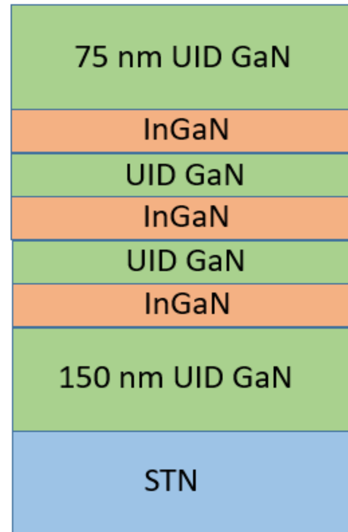

Figure 14. Epitaxial structure of Reference Sample B.

For N-polar films, Reference Sample C was grown and was identical in structure to Refence Sample B, but on a N-polar GaN on sapphire substrate grown by MOCVD with a 4° miscut. This substrate was generously provided by Dr. Stacia Keller at UCSB.

To simultaneously investigate the effect of both growth temperature and wet vs dry growth conditions on Ca incorporation, Samples D and E were grown, shown in Figure 15. Both samples had the same epitaxial structure, but Sample D was grown at 720 °C, and Sample E was grown at 765 °C. Each sample consisted of 100 nm wet UID GaN buffers followed by 200 nm of dry UID GaN, followed by 200 nm wet UID GaN. A thin (~6 nm) AlGaN maker layer was grown between the layers to help identify them in the SIMS analysis. An N-polar structure (Sample F) identical to Samples D and E was also grown at 720 °C on the previously mentioned N-polar GaN on sapphire substrate with 4° miscut.

Figure 15. Epitaxial structure for Samples D and E. Sample D was grown at 720 °C, and Sample E was grown at 765 °C.

Finally, a series of samples was grown on Ga-polar STN substrates with Ga-polishing employed at the regrowth interface to determine if this cleaning method was effective for Ca. Including Reference Sample A with zero cycles of Ga-polishing, samples G, H, and I had 2, 5, and 10 cycles of Ga-polishing, respectively. The procedure for Ga-polishing was carried out at 720 °C. Ga was deposited for 30 s while the decreasing intensity of the RHEED signal was monitored. After 30 s, the cell was shuttered and the adlayer was thermally desorbed while the intensity of the RHEED signal increased. The adlayer was considered to be thermally desorbed when the RHEED signal had stopped increasing and had reached a constant value. Then this process was repeated for the prescribed number of cycles. After this the growth proceeded the same as Reference Sample A. For each sample between 550 – 700 nm was grown after the Ga-polishing.

Prior to SIMS analysis Au was deposited on the surfaces of the samples to prevent charging in the SIMS chamber. SIMS analysis was performed on all samples at a mass-resolving

power (MRP) of 3200 for each sample to exclude masses from the conflicting atomic arrangement Si-C. Before selecting an area on each sample to perform the SIMS analysis, the Ca concentration was imaged over a wide area. From here it was easy to see Ca “hot spots” on the surface of the sample. Some areas of the film surface had higher levels of Ca than others. The final area chosen to perform the SIMS measurement was one of the areas with low Ca coverage, in order to avoid Ca from the surface around the SIMS crafter interfering with the measurement.

2.3 Results

Growth temperature, wet vs dry growth, and substrate orientation

SIMS results for Reference Sample A are shown in Figure 16. The bulk Ca concentration in the PAMBE-grown GaN is in the mid 10^{14} cm^{-3} and approaching the noise level of the SIMS system, which matches the Ca levels in the MOCVD-grown substrate. When determining how to compare Reference Sample A to the Ga-polishing series, this study will compare not just the bulk concentration of Ca in the film, but also the surface coverage of Ca at the regrowth interface. To calculate the surface coverage of Ca, the SIMS profile was integrated within 50 nm before and after the peak Ca concentration. For Reference Sample A the surface Ca concentration at the regrowth interface was 4.54×10^{13} cm^{-2}.

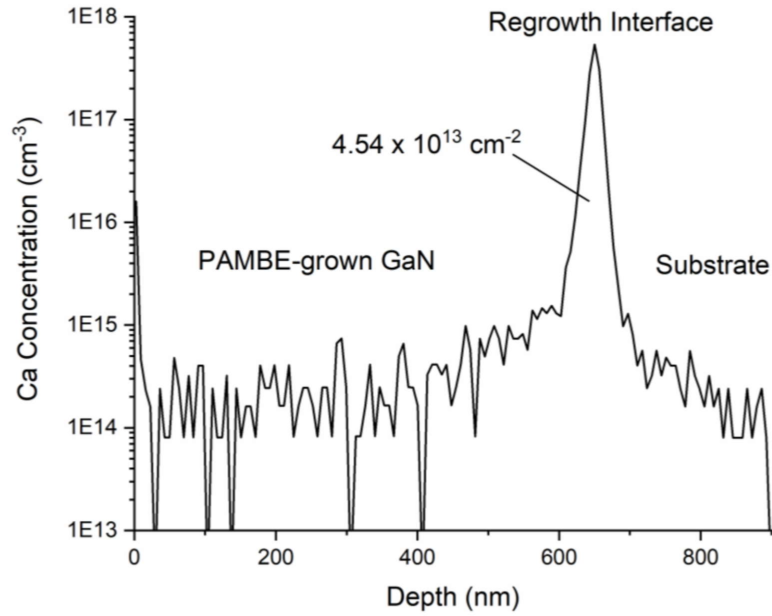

Figure 16. Ca concentration from the SIMS analysis from Refence Sample A.

SIMS results for Reference Sample B are shown in Figure 17. A reference In signal is shown to indicate the position of the QWs. Unlike Ref. [24], the bulk Ca concentration does appear to increase in the low temperature InGaN MQW region. In fact, the bulk Ca concentration is relatively constant in the film and matches that in the substrate.

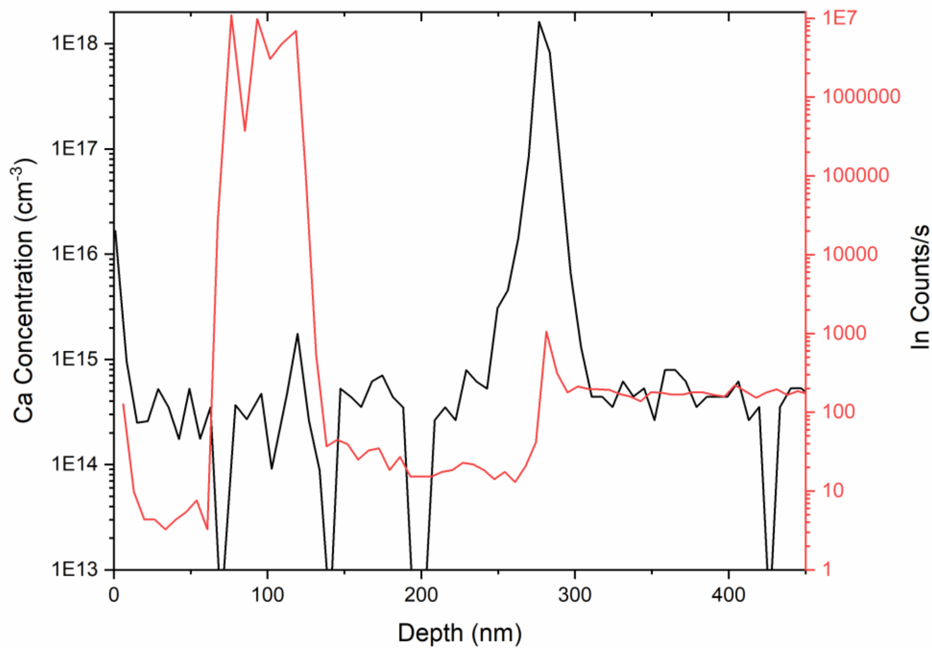

Figure 17. Ca concentration from the SIMS analysis of Reference Sample B, grown on a Ga-polar STN substrate. The reference In signal is shown in red to mark the location of the MQW region.

SIMS results for Reference Sample C (the N-polar sample) are shown in Figure 18. Unlike in Reference Sample B, this film does appear to have bulk Ca levels that are much higher than the MOCVD-grown substrate. The bulk Ca concentration in the UID GaN region are ~ 10^{16} cm^{-3}. In this sample there does appear to be a slightly higher Ca concentration in the InGaN/GaN MQW region, unlike in Reference Sample B, however the bulk Ca concentration is not lower in the GaN region after the MQW region than before it.

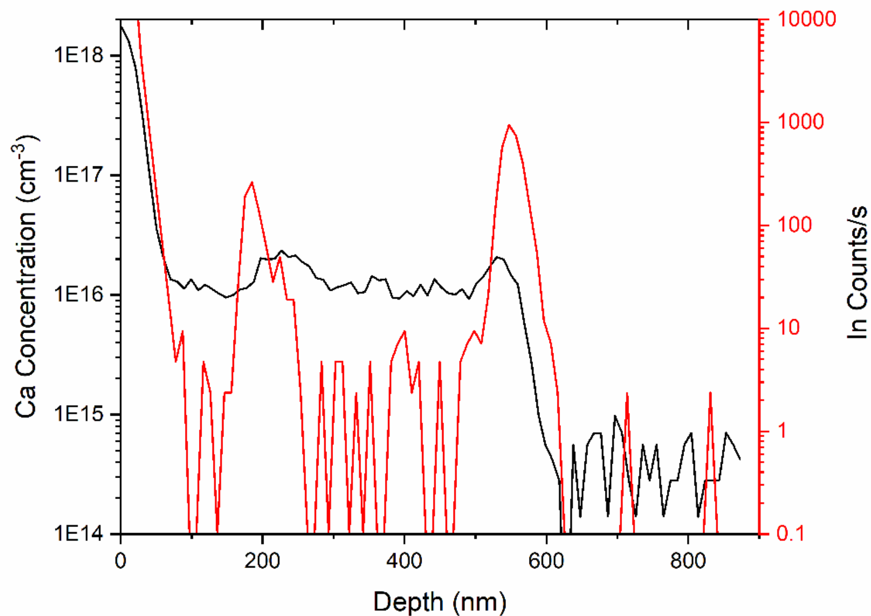

Figure 18. Ca concentration from the SIMS analysis of Reference Sample C, grown on N-polar GaN on sapphire substrate. The reference In signal is shown in red to mark the location of the MQW region.

SIMS results from Samples D and E are shown in Figure 19 and Figure 20, respectively. For both plots the reference Al signal from the SIMS measurement is included in red to indicate the position of the AlGaN marker layers. Neither sample shows a difference in the Ca concentrations between the wet GaN and dry GaN regions. In both samples the Ca levels in the PAMBE-grown film are similar to that in the MOCVD-grown substrate. Comparing the two samples to get an indication of the effect on growth temperature on Ca incorporation does not reveal much of an effect either. Both Sample D grown at 720 °C and Sample E grown at 765 °C have bulk Ca levels in the mid to high 10^{14} cm^{-3} range.

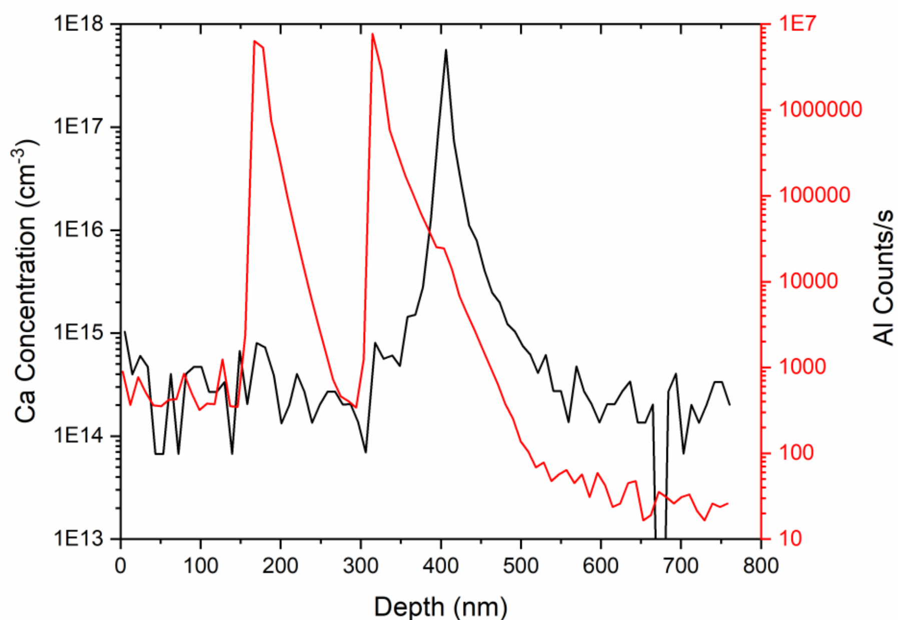

Figure 19. SIMS analysis from Sample D, grown at 720 °C. The reference Al signal from the SIMS is in red to show the AlGaN marker layers.

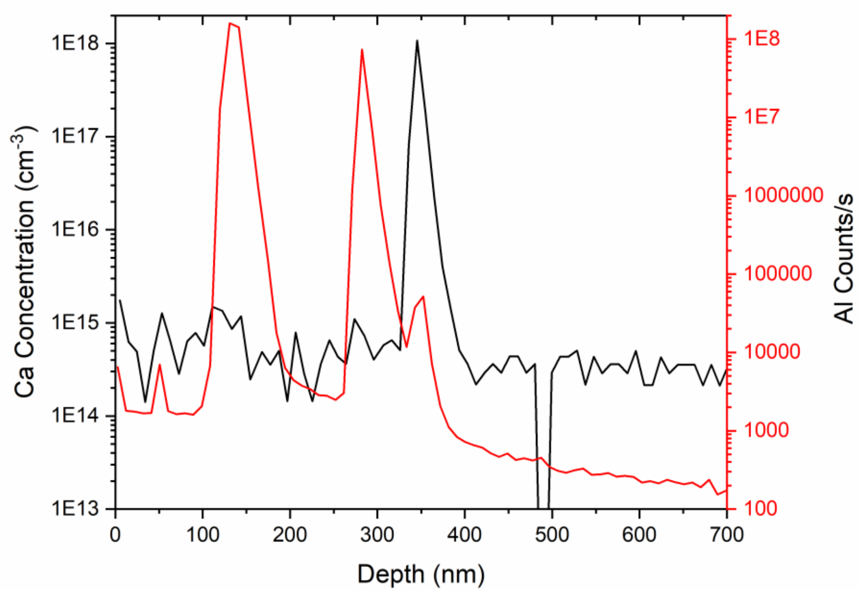

Figure 20. SIMS analysis from Sample E grown at 765 °C. The reference Al signal is in red to show the position of the AlGaN marker layers.

SIMS results for Sample F – which is equivalent to Sample D, but grown on an N-polar substrate – is shown in Figure 21. This film shows an overall higher bulk Ca concentration than Reference Sample C. It does appear that there could be slightly more Ca incorporation in the wet GaN region of the film than in the dry GaN region, but this effect is small.

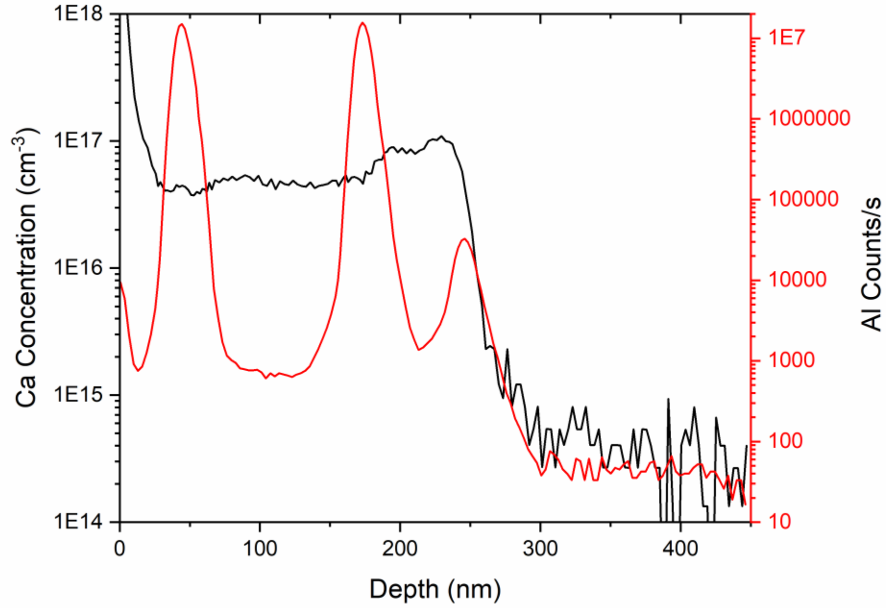

Figure 21. SIMS results for Sample F, grown at 720 °C on an N-polar substrate. The Al reference signal from the SIMS measurement is in red to show the position of the AlGaN marker layers.

Ga-polishing

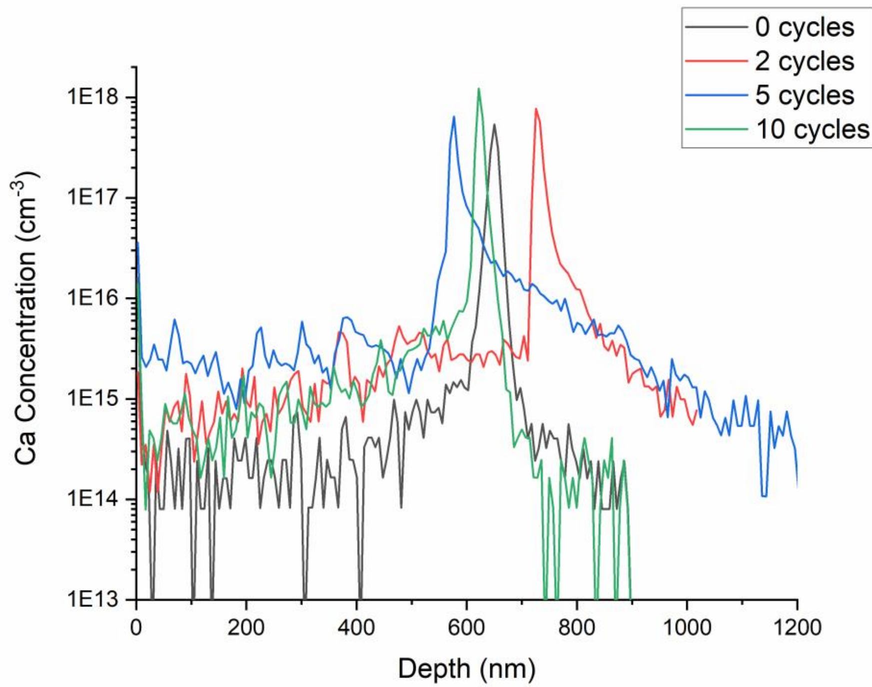

Figure 22. Ca concentration from SIMS for the Ga-polishing series.

SIMS results for the samples in the Ga-polishing series are shown in Figure 22. These data are somewhat difficult to interpret because using different metrics results in different conclusions. Three values were analyzed for each sample in the Ga-polishing series: the peak bulk Ca concentration at the regrowth interface, the surface Ca concentration at the regrowth interface, and the average Ca concentration in the bulk of the PAMBE-grown material. These values are shown in Table 1.

Table 1. Ca concentration data for the Ga-polishing series.

Sample	# Cycles of Ga-polishing	[Ca] at regrowth interface (cm^{-3})	Surface [Ca] at regrowth interface (cm^{-2})	Average [Ca] in the bulk (cm^{-3})
Reference Sample A	0	5.40×10^{17}	4.54×10^{13}	2.5×10^{14}
G	2	7.73×10^{17}	1.34×10^{12}	1.9×10^{15}
H	5	6.43×10^{17}	1.27×10^{12}	3.0×10^{15}
I	10	1.23×10^{18}	1.71×10^{12}	1.5×10^{15}

From Table 1, the bulk Ca concentration at the regrowth interface increases with more cycles of Ga-polishing. The average Ca concentration in the bulk PAMBE-grown material is lowest in Reference Sample A, which has no Ga-polishing, then does not follow a trend for samples G-I. Only the surface Ca concentration at the regrowth interface decreases with the addition of the Ga-polishing procedure. Between zero and two cycles of Ga-polishing the surface Ca concentration decreases by more than 30 times, but additional cycles of Ga-polishing do not have much effect.

2.4 Conclusions

Growth temperature, wet vs dry growth, and substrate orientation

Based on this study, growth temperature and the presence of a Ga-adlayer do not appear to affect Ca incorporation on Ga-polar substrates in PAMBE growth. Additionally, overall Ca levels in bulk Ga-polar films show much lower levels of Ca incorporation overall than reported for NH_3-MBE grown films. It should be noted that in several SIMS results presented in this study the Ca concentration levels are approaching the detection limit of the Cameca SIMS instrument used to collect the data. It is possible that with a more sensitive instrument that could

distinguish lower Ca concentrations a clearer difference between regions grown at different temperature and with and without adlayers could be identified.

Since overall Ca levels are low (generally in the 10^{14} cm^{-3} range) in the Ga-polar films in this study, Ca may not play as large a roll as a SRH non-radiative recombination center in PAMBE devices as in NH_3-assisted MBE devices. It should be noted however that even 10^{14} cm^{-3} of an SRH center could still have some impact on internal quantum efficiency. These results pose the question as to why Ca levels are so much lower in PAMBE grown III-N layers as compared to NH_3-Assisted MBE grown layers, even when both techniques are using the same substrates and cleaning procedures. One hypothesis could be that since PAMBE growth takes place at lower overall temperatures (around 100 °C lower), the majority of the Ca present on the substrate surface is almost entirely consumed in the first few nm of PAMBE buffer growth, leaving very little left to incorporate into subsequent layers.

Ca incorporation, much like other impurity incorporation, does depend on substrate orientation. Ca incorporation is around two orders of magnitude higher in N-polar films than on Ga-polar films (10^{16} cm^{-3} range in N-polar films vs 10^{14} cm^{-3} range in Ga-polar films). Although N-polar substrates are not typically used for optoelectronic devices due to this proclivity for greater impurity incorporation, it may still be desirable in certain applications to minimize Ca incorporation for other reasons, such as to improve contact resistivity [30]. These results indicate that Ca could be the explanation for the low luminescence efficiencies historically seen from N-polar optoelectronics. Luckily, this study does indicate a path towards reducing Ca in N-polar films. There is a slight increase in Ca concentration in Figure 18 between the thicker GaN buffer and the InGaN/GaN MQW region ($\sim 1 \times 10^{16}$ cm^{-3} in the buffer compared to $\sim 2 \times 10^{16}$ cm^{-3} in the MQW). Further studies are needed to determine if this increase is in fact real, and if it is due

to the change in growth temperature or if it is related to the InGaN alloy. The use of InGaN, AlGaN, or AlN underlayers in N-polar films could be the solution to reducing Ca (and other impurity) incorporation in critical device layers. Ref. [31] reports the use of an AlN initiation layer on N-polar films primarily to improve surface morphology, but also mentions that SIMS results indicate the underlayer was successful in trapping Si, O, and C. Future studies of such underlayers should examine Ca as well in N-polar films.

Ga-polishing

The data in Table 1 show mixed results on the efficacy of Ga-polishing in removing Ca from the surface of substrates prior to film growth. Based on the calculated surface coverage of Ca at the regrowth interface, it does seem that as little as 2 cycles of Ga-polishing is successful at removing Ca. However, this did not translate into lower bulk Ca levels in the remainder of the GaN film grown. It remains unclear why a lower starting Ca surface coverage would not lead to reduced Ca levels in the bulk. Based on these results, Ga-polishing prior to film growth could be useful in applications where low impurity incorporation at the regrowth interface is necessary. However, for vertical transistor structures that rely on semi-insulating buffers to compensate shallow donors that naturally occur at the regrowth interface, the presence of Ca could be useful since it has been calculated to be a deep acceptor at 1.01 eV above the valence band in pure GaN [20].

Chapter 3: Strategies for reducing impurities in regrown PAMBE devices

3.1 Introduction

Impurities on wafer surfaces originating from exposure to atmosphere

The motivation for the removal of these impurities, and Si specifically, is to achieve regrown GaN vertical transistor devices with high reverse breakdown voltages. In the drift region of these devices it is necessary to have extremely low, uniform background doping. To determine the baseline material quality of UID GaN grown by the PAMBE GenII used in this study, SIMS and Hg probe capacitance-voltage (CV) measurements were performed. For the SIMS sample a stack was grown with four thick layers of UID GaN at four different growth conditions of interest. The growth conditions are shown alongside the SIMS in Figure 23. The results show very low background O and C in the PAMBE grown films. O and C levels both increase with growth rate. Since both of these species increase with growth rate, they can compensate one another, maintaining a low net N_D-N_A at high growth rates. Figure 24 shows the N_D-N_A calculated from the Hg probe CV data for the growth rate corresponding to Layer 2 in Figure 23. For this sample N_D-N_A ~ 2×10^{16} cm^{-3}, which correlates to the O levels in Figure 23.

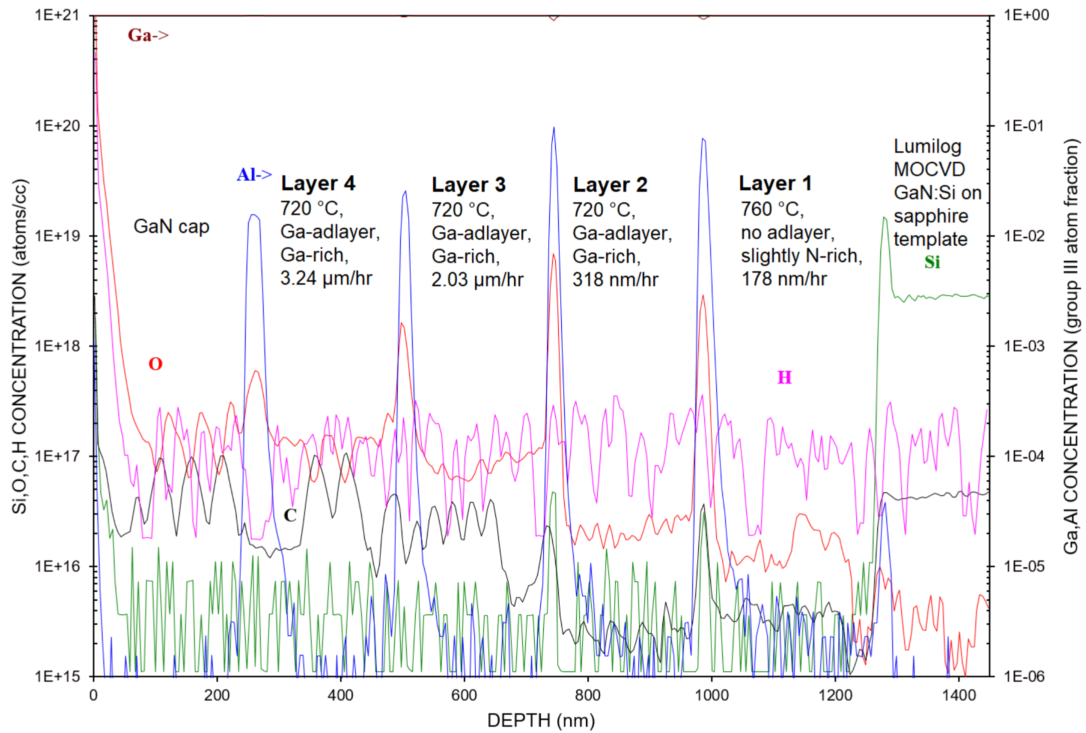

Figure 23. SIMS analysis from the PAMBE GenII system showing excellent background impurity incorporation. O and C levels increase with growth rate but compensate one another to keep N_D-N_A low. Unlike the SIMS data presented elsewhere in this work, this analysis was performed by EAG Laboratories, which has a lower sensitivity to atmospheric impurities than the Cameca SIMS at UCSB.

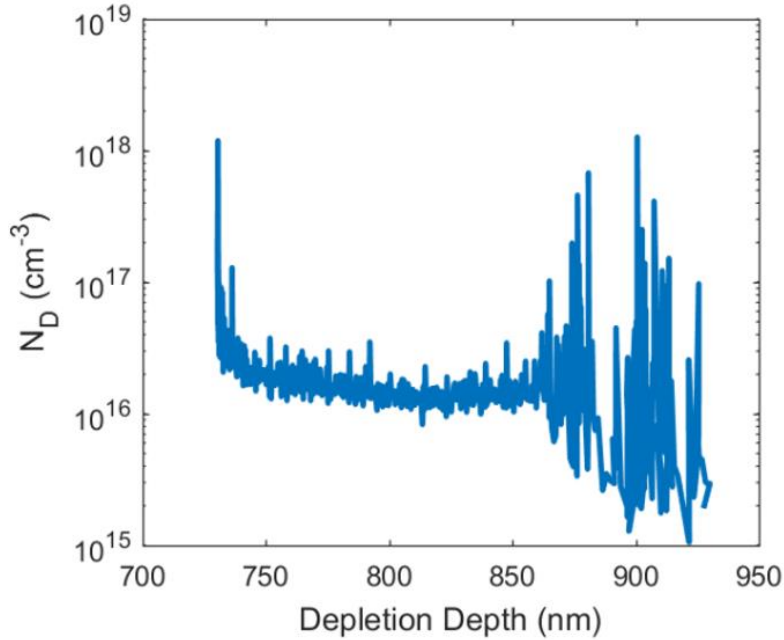

Figure 24. Hg probe CV data of UID GaN grown in the PAMBE GenII with the growth conditions of layer 2 in Figure 23 showing a net N_D-N_A around 2×10^{16} cm^{-3}.

Once the background doping level of the UID GaN grown on the PAMBE GenII system was confirmed to be low, the focus shifted to achieving a clean regrowth interface on samples that required excursions into atmosphere for processing before growth of the remainder of the device. A test sample was grown consisting of approximately 600 nm of UID GaN on a STN template. The sample was then removed from the MBE system and placed in a dry box overnight. The following day the sample was loaded back into the MBE system and outgassed following the standard protocol. In the growth chamber the sample was Ga-polished 3 times according to the procedure outlined in Chapter 2. Then another 400 nm of UID GaN was grown on top. SIMS results of the Si, C, and O profiles are shown in Figure 25. Ga-polishing was successful at almost completely eliminating the spikes of O and C at the regrowth interface, but there remains a large Si spike.

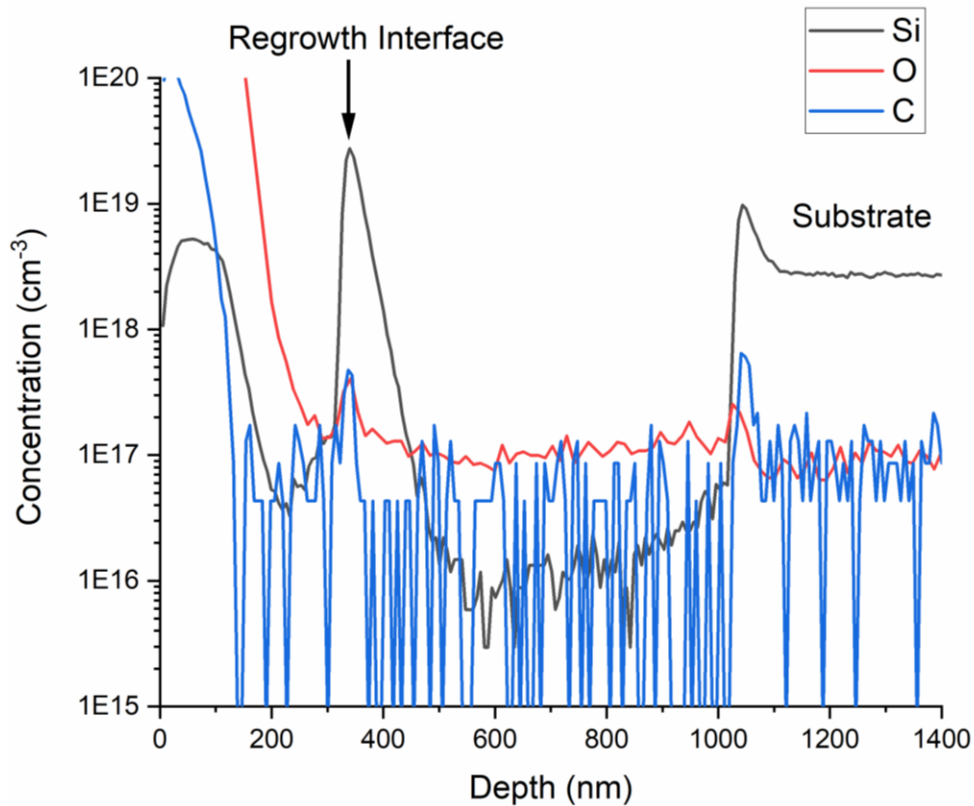

Figure 25. SIMS profile of the Si, O, and C content for a test sample with a regrowth interface. Ga-polishing was successful at almost totally removing a spike of O and C from the regrowth interface, but not Si.

This finding was consistent with reports of Ga-polishing in the literature [29]. In addition to Ga-polishing to remove O and C from sample surfaces, cyclical decomposition and growth techniques have also shown to eliminate spikes of these elements [32]. Figure 26 shows the growth rate (g.r.) and thermal decomposition rate (d.r.) used in Ref. [32] to clean the regrowth interface before the final HEMT device was grown. The SIMS results are shown in Figure 27. The treatment was successful at almost completely eliminating the O and C spikes compared to the reference sample, but the Si spike was not affected.

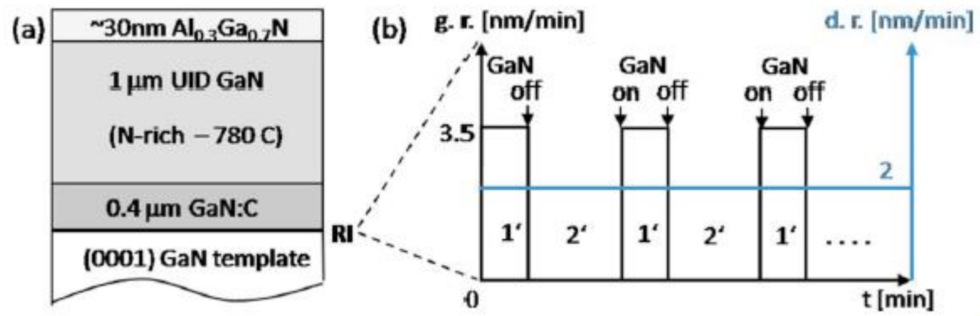

Figure 26. Schematic from Ref. [32] showing the treatment of cycles of growth and thermal decomposition used before growth of the HEMT device. This procedure was performed at 780 °C.

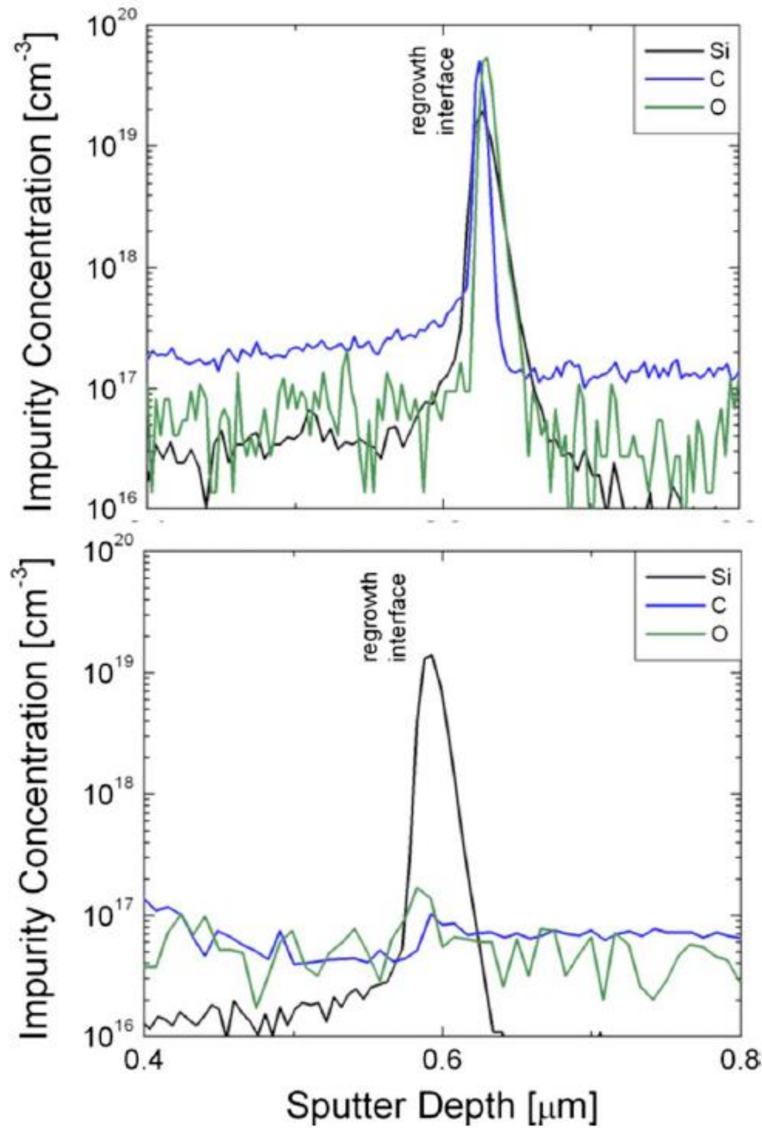

Figure 27. SIMS results from Ref. [32] showing that the O and C spikes in the top reference sample with no treatment are almost completely eliminated in the bottom sample that received the cyclical growth and decomposition treatment. Si incorporation does not appear to be affected by the treatment procedure.

Based on the tests performed in this work and the available literature, Si contamination was targeted as the main issue for regrown devices. Thus, methods for removing Si from the surface of wafers, or preventing Si from accumulating on interfaces of interest was the main goal of this chapter. There are likely to be other species (such as the Ca discussed in Chapter 2) on

wafer surfaces that are not removed by Ga-polishing or other existing cleaning methods and may negatively impact regrown devices, but the very shallow donor level of Si makes it an especially detrimental contaminant in the otherwise very low doped drift regions of the target device.

Inspiration for cleaning methods for wafer surfaces came from knowledge of other semiconductor materials systems. Cleaning of the surface oxide from heated GaAs wafers by H-radical sources is standard in the UCSB MBE lab on other MBE systems. This method is thought to work via the formation of H_2O which is then vaporized from the heated wafer surface. H-radicals have also been shown to etch amorphous Si [33]. While it is unknown what form the Si takes at the GaN wafer surface (elemental Si, SiO_2, etc.), proposed reactions to create volatile Si species are $Si + 4H^* \rightarrow SiH_4$ and $SiO_2 + 2H^* \rightarrow SiO + H_2O$.

It would also be of interest to use a capping method to prevent Si and other impurities from collecting on a regrowth interface. This would eliminate the need for additional cleaning procedures. Several capping layers have been used in the III-As material system for many years. Regardless of which material is chosen as the capping layer the principle of this method is the same. After the growth of the last epitaxial layer in the device prior to the regrowth, a capping material is deposited. This material thermally decomposes at a lower temperature than the growth temperature for the layers in the device. After the external processing is complete, the sample is placed back in the MBE system to regrow the remainder of the device. During the heating of the sample to the growth temperature for the remaining layers of the device the capping layer is thermally decomposed and desorbed from the sample surface. In the III-As system capping materials that have been used are As[34], Sb[35], and InAs[36]. These capping methods typically function to prevent exposure of the interface of interest to atmosphere to prevent formation of the native oxide that forms on GaAs.

To find a suitable capping material for the III-N system it is best to start with materials that PAMBE III-N MBE systems are already capable of growing. Since the group V source N is not a solid, there is no analogous capping method to As or Sb used in the III-As system. However, InN is suitable as an analogous capping layer to InAs in the III-As system. InN decomposes at a much lower temperature than GaN in vacuum. The growth and thermal decomposition of InN has been characterized extensively in the literature by previous growers on the PAMBE MBE system used in this study.

InN begins decomposing in vacuum above 435 °C [17], compared to around 720 °C for GaN [37]. Like GaN, InN decomposes congruently. When the In-N bonds decompose, N will leave the sample surface as N_2, leaving In to collect and eventually form droplets. The reaction for this decomposition is $2InN(s) \rightarrow 2In(l) + N_2(g)$. As the sample temperature is increased beyond 435 °C, the In droplets on the surface begin to desorb. Ref. [17] reports that all In accumulated from the decomposition of a 500 nm thick InN film was desorbed by 627 °C. This decomposition and desorption can be monitored via the RHEED signal as shown in Figure 28. As the In adlayer forms on the surface the RHEED signal decreases in intensity. The intensity reaches a minimum when droplets are formed, then begins to increase again as the droplets are thermally desorbed.

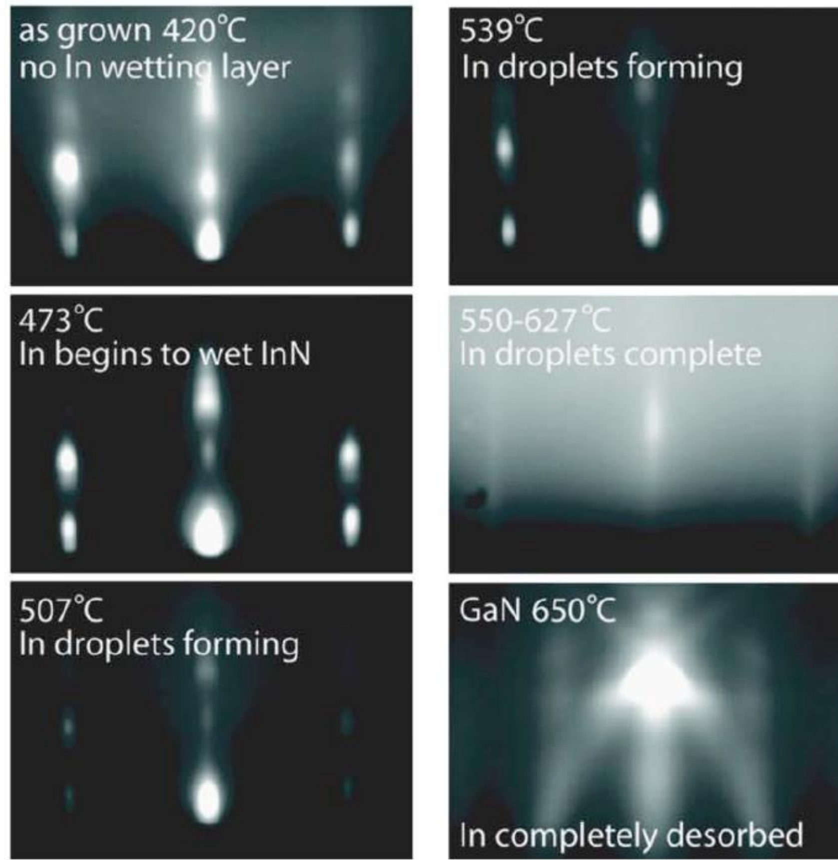

Figure 28. RHEED signal from Ref. [17] showing the decomposition of an InN film as the temperature is increased from the growth temperature of 420 °C to 650 °C. First an In wetting layer forms, followed by In droplet formation. Finally, the In droplets are thermally desorbed leaving a clean GaN surface from the substrate.

Although PAMBE III-N systems are unique in that it is possible to grow smooth, high electron mobility InN films on GaN substrates, the quality of an InN capping layer does not need to meet the same standard as epitaxial layers in devices. If impurities that collect on the InN cap surface can be thermally desorbed with the InN capping layer, it may be possible to prevent crucial GaN and AlGaN interfaces from becoming contaminated prior to regrowths.

3.2 Experimental

To determine if cleaning or capping methods are successful at removing Si from the surface of wafers or preventing its accumulation it is necessary to know how much Si was on the wafer surface prior to any cleaning treatment. If samples were allowed to contaminate naturally in atmosphere, the amount of Si that segregated on the wafer surface would not be controllable. To avoid this, samples were intentionally contaminated *in situ* in the PAMBE growth chamber. To measure the atomic flux of Si from the effusion cell on the PAMBE growth chamber a reference sample (shown in Figure 29) was grown. The temperature of the Si cell was held constant at 1300 °C. First a 200 nm GaN buffer was grown under standard Ga-rich conditions at 720 °C under a Ga adlayer on an STN substrate. Then the Ga adlayer was desorbed completely as determined by the RHEED intensity increasing and then leveling off. Next, the sample was exposed to a Si flux for 10 s. Then another 200 nm of GaN was grown. The Si deposition process was repeated, this time exposing the sample to Si for 60 s. Then a 200 nm GaN cap was grown on top.

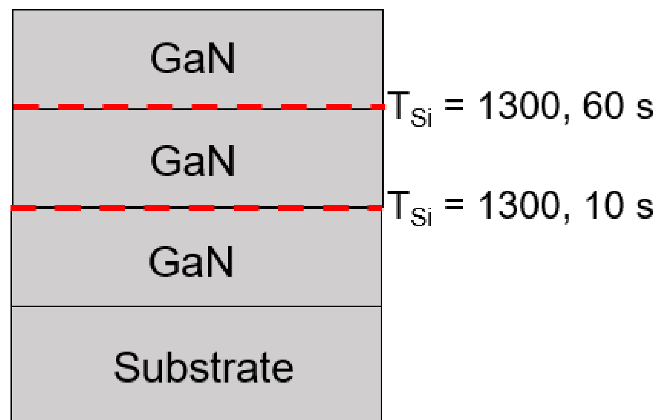

Figure 29. Sample schematic used to measure the atomic flux of Si from the effusion cell on the PAMBE growth chamber.

The sample was then removed from the PAMBE system and analyzed via SIMS. The Si SIMS concentration is shown in Figure 30. The SIMS data shows two spikes of Si concentration corresponding to the two Si depositions in the MBE chamber. The atomic flux of Si was calculated assuming that all of the Si deposited on the sample surface incorporated into the GaN layers. To get an areal concentration of Si, the two spikes were integrated from 50 nm on either side of the peak bulk Si concentration. The areal density of Si is shown for each spike. These areal concentrations were divided by the amount of time the sample was exposed to Si to find a flux. The two values were averaged, and the calculated atomic flux of Si was 1.2×10^{12} $cm^{-2}s^{-1}$.

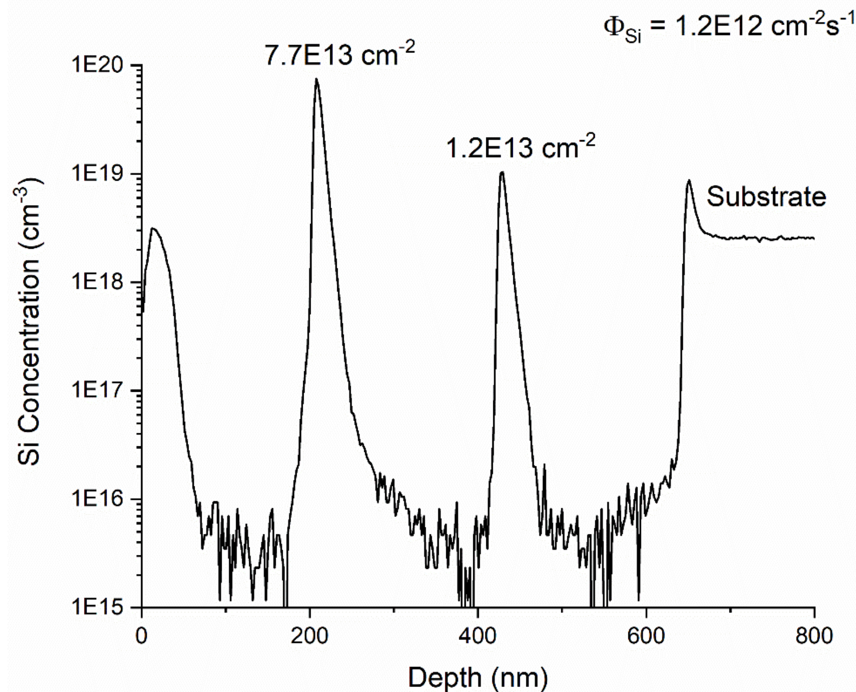

Figure 30. SIMS plot of Si concentration used to determine the atomic flux of Si from the effusion cell on the PAMBE growth chamber.

For any SIMS measurement taken with the Cameca SIMS equipment at UCSB, special care was taken whenever a measurement of atmospheric impurities (O, C, H, and Si) was performed. Since the Cameca SIMS at UCSB is a shared tool that is used to analyze a wide

variety of materials including oxides, organic materials, and other III-V semiconductors, one must be mindful of the chamber being contaminated with the atmospheric species that are being investigated in this study. The Cameca SIMS has two sources of primary ions: a solid Cs source and an O duo plasma source. The Cs source is not pure Cs, but rather has O and C present as well, so it is imperative that strong magnets be placed on the outside of the chamber along the path from the Cs source to the sample to deflect the lower mass C and O atoms and prevent them from reaching the sample and increasing the background level of the measurement.

Wherever possible samples were loaded into the SIMS system at the end of the work week on Friday, so that the analysis chamber would have two days to pump prior to the measurement of atmospheric impurities on Monday morning. A hot bake lamp in the load lock chamber was also used over the weekend to drive off adsorbed species from the sample surface. Additionally, a piece of GaAs wafer was included with the samples to be measured. Once the samples were loaded into the measurement chamber the GaAs wafer was etched with the Cs primary ion beam for approximately 30 minutes in an attempt to getter any O still in the chamber.

The etch rate used during the SIMS measurements for atmospheric species was relatively fast compared to that used for other species. Although this results in poorer depth resolution, this was chosen to ensure that atmospheric species that were adsorbed onto the sample surface around the SIMS crater did not interfere with the measurement. For samples that required analysis with both the Cs and O primary ion sources, all atmospheric measurements with the Cs source were completed first before the O source was turned on to prevent O from contaminating the chamber. Dr. Tom Mates, the SIMS scientist at UCSB, was instrumental to this process and

has spent a lot of time perfecting the measurement of atmospheric impurities with as low a background as possible.

3.2.1 H-radical cleaning

Ideally this experiment would have been carried out on one MBE system, without the H-radical cleaned interface ever coming into contact with atmosphere. However, at the time of this experiment, there was no H-radical source on the GenII PAMBE system at UCSB. The H-radical source used in this study is installed on the buffer chamber of a Veeco GenIII III-As MBE system in the UCSB MBE lab. The experimental procedure is shown in Figure 31. Two identical samples were grown. First 350 nm of GaN was grown on a standard STN substrate in the PAMBE chamber under standard Ga-rich growth conditions at 720 °C under a Ga adlayer. After the adlayer was thermally desorbed, 5×10^{13} cm^{-2} Si was deposited on the sample surface. Then the samples were removed from the PAMBE system, de-bonded from their Si wafers, and re-bonded to a smaller Si wafer that was compatible with the blocks in the III-As system.

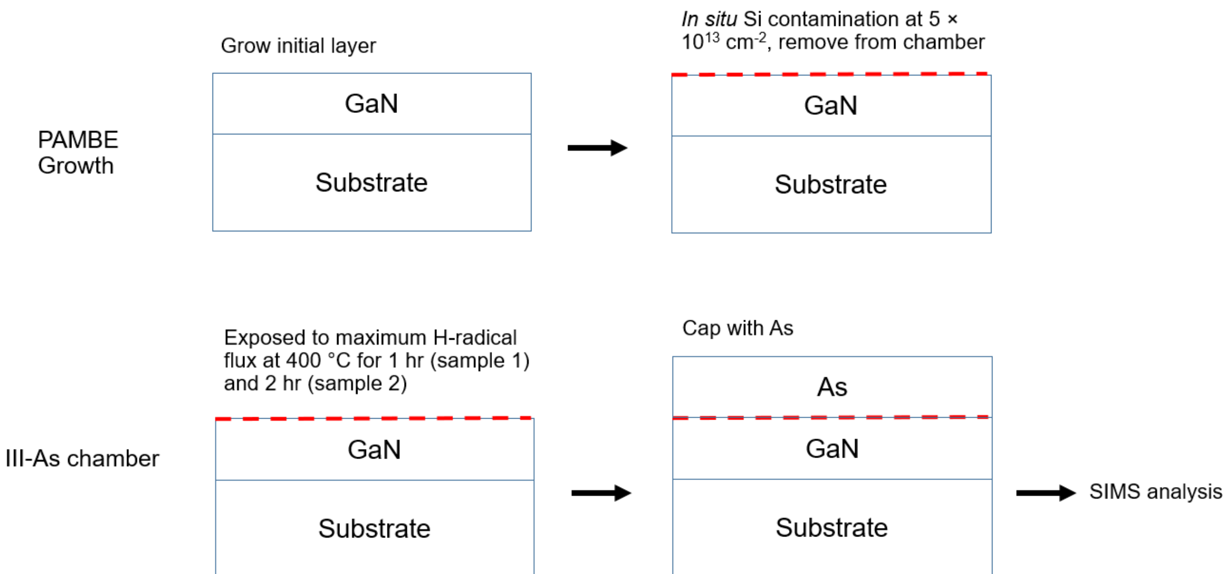

Figure 31. Procedure for H-radical cleaning experiment.

The remainder of the procedure was carried out by Zach Biegler, a student of Dr. Jim Speck with assistance from Dr. Justin Norman, Brian Haidet, and Dr. Anthony McFadden, who are familiar with the III-As system used for the H-radical cleaning. The samples were loaded into the III-As MBE system and transferred to the buffer chamber. Sample 1 was exposed to the H-radical source operated at maximum capacity for 1 hour while the sample was heated to 400 °C. Sample 2 was treated in the same way but was exposed to the H-radicals for 2 hours. Maximum capacity for the H-radical source is defined as the point at which the pressure in the buffer chamber reached into the 10^{-6} Torr range. A more quantitative measure of the flux of H-radicals was not possible due to the setup available on the III-As MBE system.

After the exposure to H-radicals, each sample was capped with As in the growth chamber to preserve the interface prior to SIMS analysis. The two samples were then loaded into the Cameca SIMS at UCSB and analyzed for Si as well as C, O, and H. To measure the surface coverage of Si on the GaN film the Si concentration profile was integrated similarly to the Ca concentration in Chapter 2.

3.2.2 InN capping

To investigate the effectiveness of an InN capping layer on regrown III-N devices to prevent critical interfaces from being exposed to atmospheric impurities, *in situ* contamination of the sample surface with Si was used similarly to the H-radical cleaning procedure mentioned previously. Instead of growing an InN cap, removing it from the PAMBE system, and allowing it to contaminate naturally in atmosphere, the *in situ* contamination procedure was done entirely in the PAMBE growth chamber.

Figure 32 shows a schematic of the InN caping procedure. Two STN wafers were solvent cleaned and loaded into the PAMBE system and baked in the buffer chamber using the standard

pre-growth procedure. In the growth chamber, an approximately 400 nm of GaN buffer was grown under standard Ga-rich conditions at 720 °C under a Ga adlayer. Next, the sample was cooled to 400 °C and an InN capping layer was grown under In-rich conditions under an In adlayer. Next 1.2×10^{13} Si/cm^{-2} was deposited on the surface of the InN to mimic atmospheric contamination with Si. Next the sample was heated back to 720 °C, which caused the InN layer to decompose. The RHEED pattern and intensity were monitored to observe the InN decomposition.

Once the intensity of the RHEED pattern was constant again (indicating that all of the InN had decomposed and all metal on the surface had desorbed), another approximately 400 nm GaN layer was grown under the same growth conditions as the buffer. Then the sample was cooled again, more InN was grown, and 7.7×10^{13} Si/cm^{-2} was deposited on the InN capping layer. The film was heated again, causing the second InN capping layer to be decomposed. Then a 400 nm GaN cap was grown. This procedure was repeated for both samples, with Sample 1 having approximately 50 nm thick InN capping layers and the second having approximately 200 nm thick InN capping layers.

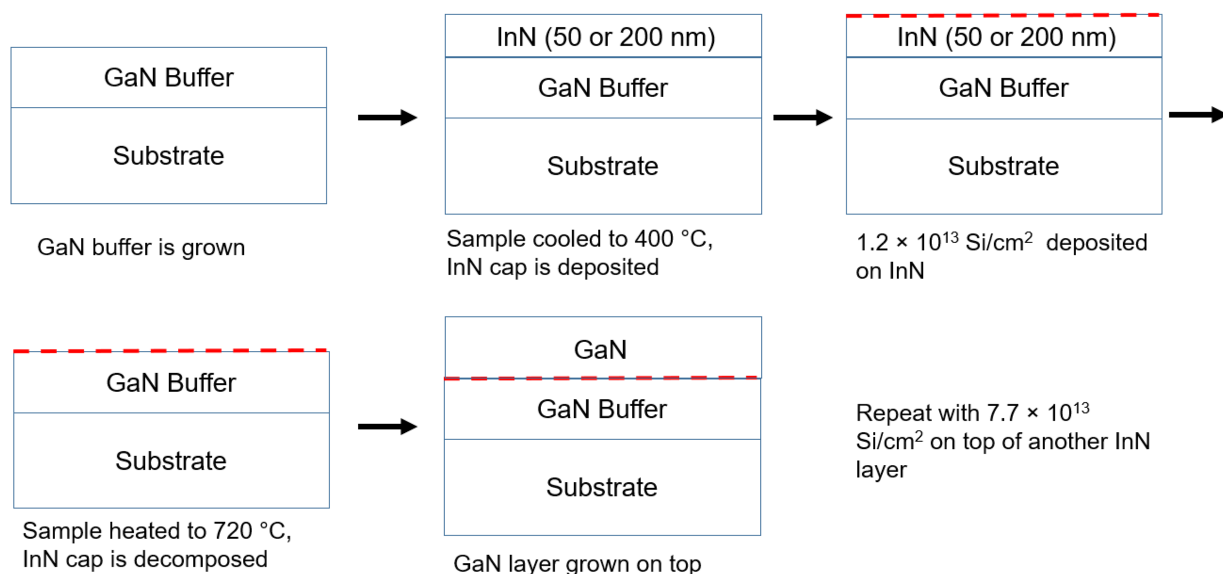

Figure 32. Schematic for the InN capping experimental procedure.

After the samples were removed from the PAMBE system they were loaded into the Cameca SIMS at UCSB where the Si concentration was measured along with In used as a reference signal. The bulk Si concentration data were integrated at the Si peaks to determine the surface coverage of Si remaining after decomposition of the InN capping layers.

3.3 Results

3.3.1 H-radical cleaning

SIMS concentration profiles of Si, C, O, and H for Sample 1 (with 1 hour of H-radical exposure) are shown in Figure 33. The areas of the As cap, PAMBE-grown GaN and GaN substrate are indicated in the figure. The integrated surface coverage of Si at the interface between the PAMBE-grown GaN and the As cap is 4.9×10^{13} Si/cm^2, which is approximately the same as the 5×10^{13} Si/cm^2 deposited in the PAMBE growth chamber. There are also spikes of C, O, and H at the interface that received the H-radical treatment.

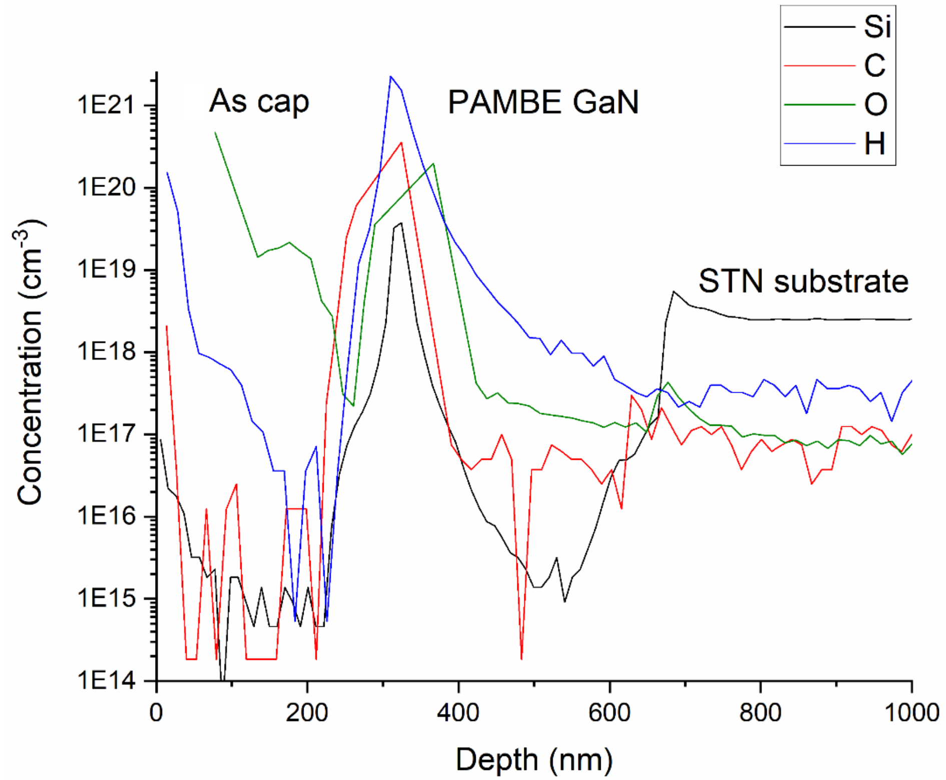

Figure 33. SIMS Results for Sample 1, which was exposed to H-radicals 1 hour. The integrated Si surface coverage calculated was 4.9×10^{13} cm^{-2}.

SIMS profiles of Si, C, O, and H for Sample 2 (with 2 hours of H-radical exposure) are shown in Figure 34. The integrated surface coverage of Si at the interface between the PAMBE-grown GaN and the As cap is 5.2×10^{13} Si/cm^2, which is approximately the same as the 5×10^{13} Si/cm^2 deposited in the PAMBE growth chamber. There are also spikes of C, O, and H at the interface that received the H-radical treatment.

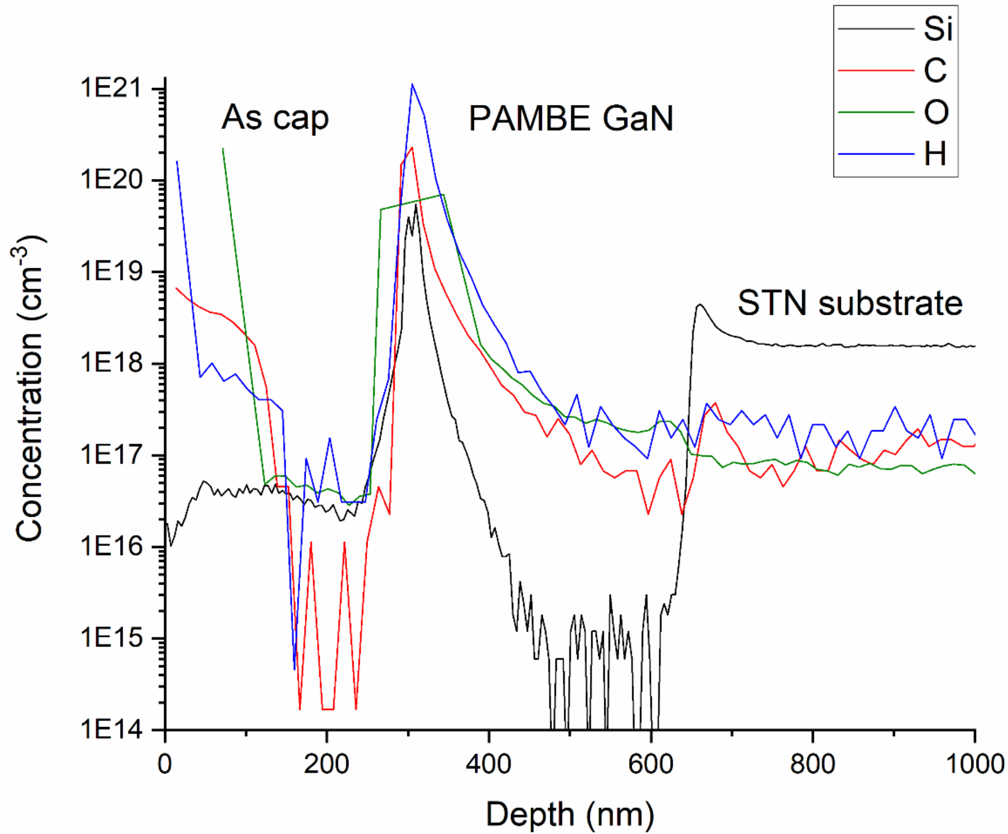

Figure 34. SIMS results for Sample 2, which was exposed to H-radicals 2 hours. The integrated Si surface coverage calculated was 5.2×10^{13} cm^{-2}.

3.3.2 InN capping

Figure 35 shows the SIMS data for Sample 1 with 50 nm InN capping layers. The spikes in Si concentration match with the trace spikes of In leftover from the InN capping layers. The Si doped GaN substrate is on the far right in the area with constant Si concentration. The Si spike closest to the substrate, which corresponds to the 1.2×10^{13} Si/cm^2 Si deposition on the first InN cap grown, has an integrated surface coverage of 1.5×10^{13} Si/cm^2. The Si spike closest to the surface, which corresponds to the 7.7×10^{13} Si/cm^2 Si deposition on the second InN cap grown, has an integrated surface coverage of 9.9×10^{13} Si/cm^2. The surface coverage of Si for both spikes is greater than the calculated amount of Si deposited in the PAMBE growth chamber.

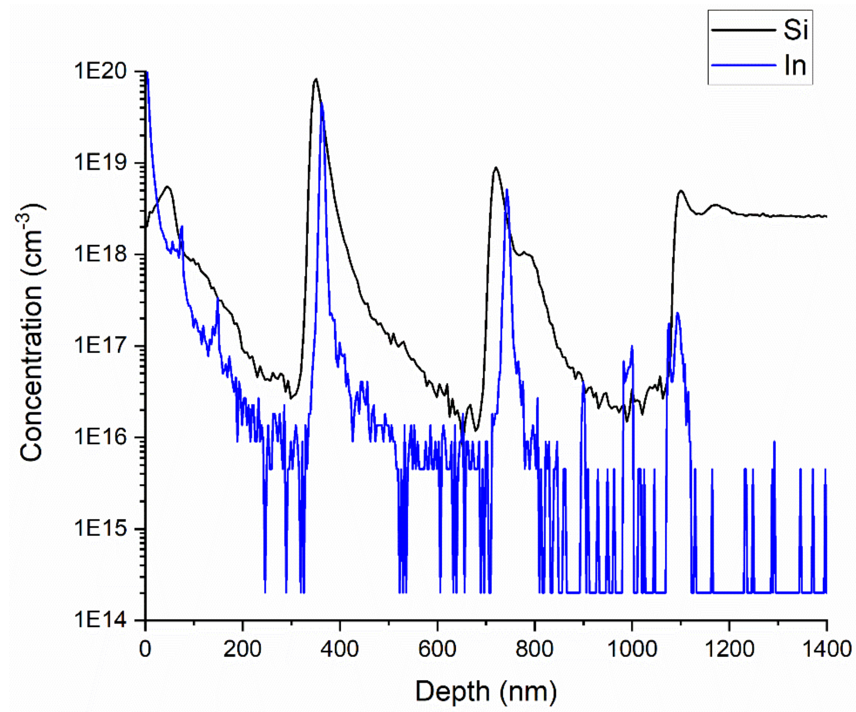

Figure 35. SIMS data from Sample 1 with 50 nm InN capping layers.

Figure 36 shows the SIMS data from Sample 2 with 200 nm InN capping layers. The Si doped GaN substrate is on the far right in the area with constant Si concentration. The Si spike closest to the substrate, which corresponds to the 1.2×10^{13} Si/cm^2 Si deposition on the first InN cap grown, has an integrated surface coverage of 2.3×10^{13} Si/cm^2. The Si spike closest to the surface, which corresponds to the 7.7×10^{13} Si/cm^2 Si deposition on the second InN cap grown, has an integrated surface coverage of 1.3×10^{14} Si/cm^2. The surface coverage of Si for both spikes is greater than the calculated amount of Si deposited in the PAMBE growth chamber.

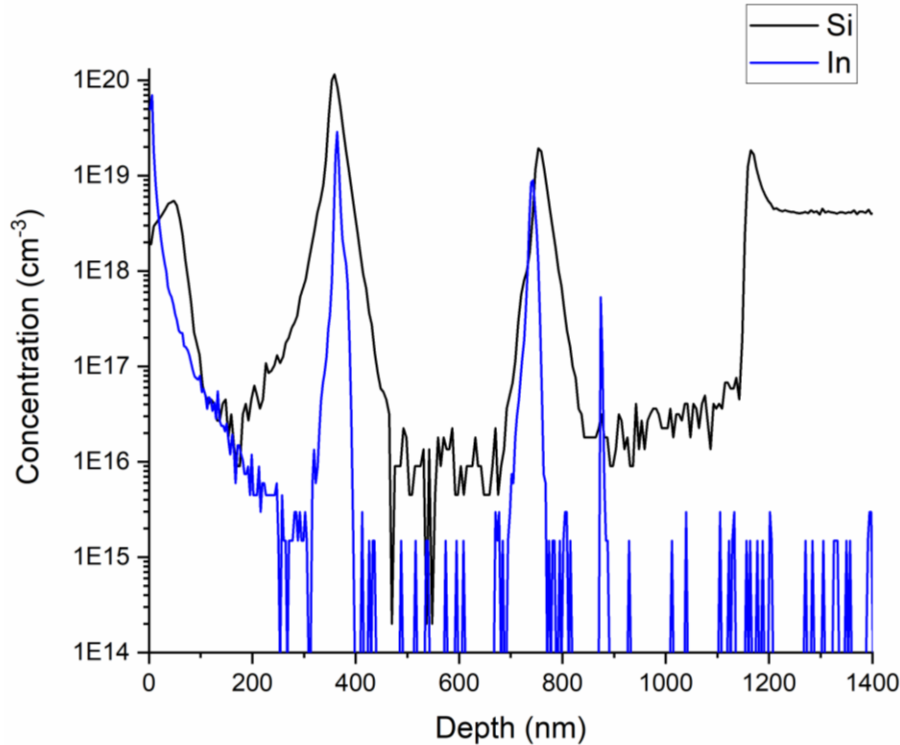

Figure 36. SIMS data from Sample 2 with 200 nm InN capping layers.

3.4 Conclusions

Though neither the H-radical cleaning procedure nor the InN capping layer investigated in this study were successful at removing surface Si contamination or preventing Si from accumulating on a regrowth interface, there is still hope that variations of these methods can still be successful. The flux of H-radicals used in this investigation were not sufficient to remove Si (or other atmospheric contaminants) from the sample surface, it is still possible that a newer H-radical source, which can provide a much higher H-radical flux, could be successful. Current work in the Speck group is underway to test a higher flux H-radical source as well as a high flux O-radical source. The current hypothesis is that O-radicals could form a Si sub-oxide that is volatile at lower temperatures than SiO_2. These H- and O-radical sources have been installed on the buffer chamber of the PAMBE system used in this study as of the time of publication.

Having the radical sources on the same system as the growth chamber will also improve the repeatability of these studies since a sample will not need to be exposed to atmosphere before being subjected to a radical clean.

It appears that the Si deposited in the growth chamber on top of the InN cap rides the surface of the decomposing cap layer and re-deposits on the GaN below. Even though in this study InN capping layers did not result in prevention of Si from reaching a GaN interface, this capping method should be investigated for removal of other contaminants (Ca and atmospheric contaminants such as O, C, and H). It is likely that the desorbing of the In metal from the surface during the decomposition of the InN cap could work in a way similar to Ga-polishing and be useful for removing certain species from a regrowth surface. Additionally, an InN capping layer could also be useful for protecting an important GaN interface from processing-induced damage in regrown devices. Energized etches used in the processing of III-N are known to cause damage to the material and using a sacrificial InN cap could prove useful to protect a critical GaN surface.

Chapter 4: Improving impurity incorporation in InGaN by using high N* fluxes

4.1 Introduction

III-N multi-quantum well (MQW) light-emitting diodes (LEDs) with $In_xGa_{1-x}N$ active regions have enabled energy-efficient white lighting sources. While all commercial devices today are grown by metal organic chemical vapor deposition (MOCVD), plasma-assisted molecular beam epitaxy (PAMBE) offers a unique opportunity to grow $In_xGa_{1-x}N$ with higher In-content than NH_3-based growth methods. Unlike MOCVD and NH_3-MBE, PAMBE does not rely on the thermal decomposition of NH_3 to supply nitrogen to the growth surface. This enables growth at lower temperatures, and thus higher In content $In_xGa_{1-x}N$, and even pure InN, is readily achievable.

The drawback of lower temperature growth, however, is a decrease in adatom mobility on the film surface, making smooth morphologies difficult to achieve. To overcome this, $In_xGa_{1-x}N$ is typically grown under a highly-mobile saturated 2.5 monolayer In adlayer that acts a surfactant by increasing the adatom mobility [17]. The adlayer presence also has the added benefit of creating a nearly constant alloy composition at a given temperature. PAMBE also enjoys low background impurity concentration as well as active as-grown p-GaN. This enables p-GaN to be placed anywhere in an epi-structure, enabling device designs that are unavailable to MOCVD due to the challenges of activating the Mg acceptors for buried GaN:Mg layers. Despite the advantages of PAMBE growth, attempts at an all-PAMBE nitride LEDs have been few, and published efficiency values have been poor [38–40].

Regardless of technique, the growth of $In_xGa_{1-x}N$ alloys is challenging due to the large difference in thermal stability of its constituent materials, GaN and InN. In vacuum, In-N bonds begin to decompose at 435 °C [17], whereas Ga-N bonds do not decompose for temperatures lower than ~720 °C [37]. This means that the optimal growth temperature for $In_xGa_{1-x}N$ is very different from that of GaN. For PAMBE, $In_xGa_{1-x}N$ growth typically takes place between 500 °C - 650 °C in a regime where In-N bonds are actively decomposing. The alloy composition is thus extremely temperature dependent. Since the Ga-N bonds are significantly more stable than In-N bonds, the supplied Ga-flux (Φ_{Ga}) to the $In_xGa_{1-x}N$ must be less than the supplied active nitrogen flux (Φ_{N*}), otherwise no In will incorporate in the growing layer [41]. For $In_xGa_{1-x}N$ growth under a saturated In wetting layer, to very good approximation, the Indium composition x in the $In_xGa_{1-x}N$ film is determined by the growth temperature.

The exact identity of the active nitrogen species that participates in III-N growth from RF plasma units remains a matter of debate. Carefully conducted appearance mass spectroscopy (AMS) experiments have indicated that the species that reaches the substrate is atomic N [11], however optical emission spectroscopy (OES) from the back viewport of the plasma has indicated that a meta-stable excited N_2 molecule is also present [12,13]. It is beyond the scope of this report to make a determination about the identity of the active species, and for simplicity the active nitrogen will be represented as N*.

Two methods of growing $In_xGa_{1-x}N$/GaN quantum well/quantum barrier (QW/QB) active regions via PAMBE currently exist. In one method, the sample is heated and cooled between layers. $In_xGa_{1-x}N$ QWs are grown at a low temperature, then a thin, low temperature GaN “cap” is grown on the $In_xGa_{1-x}N$ layer before the sample is heated to suppress subsequent $In_xGa_{1-x}N$ decomposition. Then the remainder of the GaN QB is grown at the higher growth temperature.

This way both the QWs and the majority of the QBs are both grown at the optimal $In_xGa_{1-x}N$ and GaN growth temperatures, respectively. These growth interrupts due to heating and cooling cycles make impurities more likely to segregate on the interfaces between layers, which can produce defects that reduce the radiative efficiency. Another method of growing a MQW region consists of growing the entire region at a lower temperature suited to $In_xGa_{1-x}N$ growth, and using two separate Ga-fluxes to modify the composition of the QWs and QBs [42,43]. In this method a constant In-flux (Φ_{In}) and Φ_{N^*} are supplied to the film while Φ_{Ga} is modulated between $\Phi_{Ga1} < \Phi_{N^*}$ for the QWs and $\Phi_{Ga2} \geq \Phi_{N^*}$ for the QBs. This method eliminates growth interrupts between layers, but at the cost of growing the GaN QBs at a temperature lower than the ideal GaN growth temperature.

Modern high flux RF plasma sources can supply over an order of magnitude greater active nitrogen flux than previously possible, enabling reported growth rates as high as 7.6 μm/hr [10] and 8.4 μm/hr [44] while supplying pure N_2 to the plasma source. Φ_{N^*} of this magnitude enables the exploration of growth regimes previously inaccessible to PAMBE III-N growth. For InN and $In_xGa_{1-x}N$ growth, increasing the N overpressure suppresses In-N bond decomposition. Modeling by Turski et al. [41] predicts that supplying an order of magnitude higher absolute Φ_{N^*} will result in approximately 10% increase the In composition in $In_xGa_{1-x}N$ films. Utilizing this high Φ_{N^*} could enable growth of $In_xGa_{1-x}N$ at higher temperatures than previously established, potentially improving the material quality and thus enabling efficient PAMBE-grown $In_xGa_{1-x}N$ based light emitters. If $In_xGa_{1-x}N$ growth could be realized at typical GaN growth temperatures, it could be feasible to grow an entire active region of an LED without growth interrupts at the growth temperature similar to that used for the highest quality PAMBE GaN grown under a saturated Ga adlayer (typically close to 720 °C).

In this work we show the effect of high active nitrogen flux on the incorporation of In into $In_xGa_{1-x}N$ films, and how that higher flux can enable $In_xGa_{1-x}N$ growth at temperatures higher than previously demonstrated for PAMBE. The effect of the high active nitrogen flux on surface morphology is also discussed.

4.2 Experimental

All samples were grown in a Varian GenII MBE equipped with two Ga Titan cells (E-Science, Hudson, WI), an In SUMO cell (Veeco, St. Paul, MN), and a modified Riber RFM50/63 RF-plasma source using nitrogen gas (99.9995% purity). The system is equipped with a reflection high energy electron diffraction (RHEED) gun for in-situ monitoring of the crystal surface. During growth, the main chamber is pumped by two cryogenic pumps and an additional ion pump is used when the system is idle. The base pressure of the main chamber is around 1×10^{-10} Torr and typical pressures during growth are in the 10^{-5} Torr range, depending on the N_2 gas flow rate.

The substrate used is a single-side polished GaN:Si on sapphire template from Lumilog St. Gobain. The back of the wafers were coated in 500 nm of Ti to improve thermal contact and to provide a black body source for the optical pyrometer to measure growth temperature. The optical pyrometer emissivity was calibrated to the melting point of Al. The template wafers were diced into 1×1 cm^2 pieces. The cleaning procedure for each sample was 3 minutes each in acetone, methanol, and isopropanol in an ultrasonic bath. Each wafer piece was then In-bonded to a lapped Si wafer and loaded into the MBE system. Each sample was outgassed for 1 hour at 400 °C in vacuum before being loaded into the growth chamber.

To quantify Φ_{N*} in terms of a GaN equivalent growth rate, a sample structure of a GaN buffer, 5 nm AlGaN layer, followed by a 100-250 nm Ga-rich GaN layer was grown for each

plasma condition. This structure was grown at 720 °C, where Ga-N bond decomposition is negligible. The thickness of the top GaN layer was then determined by measuring the thickness fringes on a high-resolution X-ray diffraction (HRXRD) ω-2θ (0002) scan. The growth thickness was then divided by the growth time to determine the growth rate. To quantify Φ_{Ga} in terms of a GaN equivalent growth rate the same structure was grown, but this time with an N-rich top GaN layer. The thickness and growth rate were determined in the same manner. This was done for a series of Φ_{Ga}. A plot of growth rate vs. Ga beam equivalent pressure (BEP) was made, and a linear relationship was fitted.

To quantify Φ_{In} in terms of an InN equivalent growth rate a series of pure InN films were grown on the GaN:Si on sapphire templates at 420 °C where In-N bond decomposition is negligible. The growth was N-rich and Φ_{In} was varied for each sample. These films were relaxed and rough (as expected), so thickness determination via HRXRD was not possible. Instead the samples were cleaved and the thickness was measured via scanning electron microscopy (SEM) in cross section. As for the Φ_{Ga} determination, a linear relationship between InN growth rate and In BEP was fitted to the data.

Fluxes given in equivalent growth rates can also be converted into atomic fluxes. One monolayer (ML) of GaN corresponds to $\frac{c_{0,GaN}}{2} = 0.259\ nm$ with 1.14×10^{15} atom/cm^2 planar density. In this work atomic fluxes are shown in parentheses beside their equivalent growth rate counterparts. One small issue of this method is that during $In_xGa_{1-x}N$ growth the c lattice spacing differs depending on the film composition x. However, since $c_{0/GaN}$ and $c_{0,InN}$ differ by approximately 10%, and the films in this study are all of lower composition ($x \leq 0.25$), using $c_{0,GaN}$ as an approximation of 1 ML will introduce only a small error.

Figure 37(a) shows the schematic for sample growth. For each sample a GaN buffer layer was first grown at 720 °C under standard Ga-rich conditions using the modulated growth technique [9]. The N_2 flow rate was 3 sccm and the plasma forward power was 200 W. This corresponded to a growth rate of about 0.4 μm/hr (4.9×10^{14} atom/cm^{2}s). A Φ_{Ga} of around 8×10^{-7} Torr beam equivalent pressure (BEP) was used, which corresponded to about 0.7 μm/hr (8.6×10^{14} atom/cm^{2}s). The sample was rotated during buffer growth at 1 rotation per minute (RPM) to ensure that a uniform thickness was deposited over the area of the sample.

After the GaN buffer growth, the temperature was decreased to the desired $In_xGa_{1-x}N$ growth temperature. Next, a coherent $In_xGa_{1-x}N$ layer was grown. The thickness of the $In_xGa_{1-x}N$ layers varied between 20-65 nm to ensure that all films were coherent. To initiate $In_xGa_{1-x}N$ growth the In shutter was opened first, and the RHEED intensity transient was monitored. When the RHEED intensity reached a minimum the Ga and N* shutters were opened. After the target growth time is reached, all shutters were simultaneously closed and the adlayer was desorbed. Figure 37(b) shows the RHEED intensity transient and shutter timing for 30 s of $In_xGa_{1-x}N$ film growth.

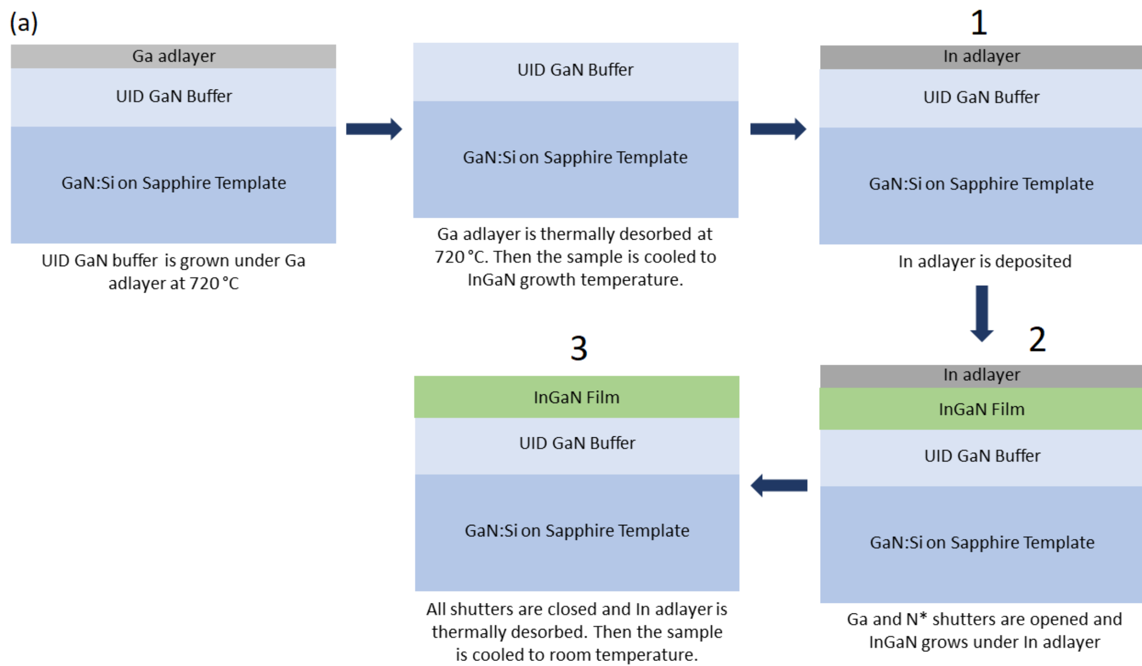

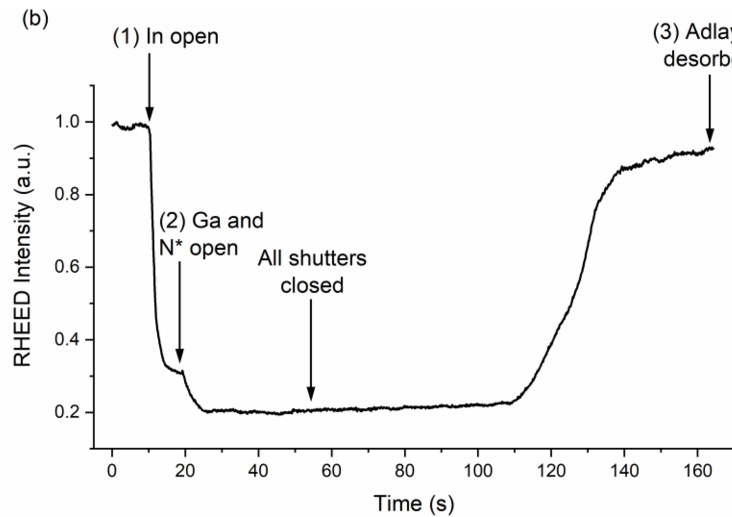

Figure 37 (a) Schematic for GaN buffer and $In_xGa_{1-x}N$ film growth. (b) RHEED intensity transient for $In_xGa_{1-x}N$ growth showing the In adlayer formation, growth of the film, and adlayer thermal desorption.

The first grown series (Series 1) was grown with a N_2 flow rate of 6 sccm and a plasma forward power of 450 W, which corresponded to a N-limited GaN equivalent growth rate of 1.5 μm/hr (1.8×10^{15} atom/cm^{2}s). $\Phi_{Ga} = 8\times10^{-7}$ Torr BEP was used, which corresponded to a Ga-limited GaN equivalent growth rate of 1.0 μm/hr (1.22×10^{15} atom/cm^{2}s). Φ_{In} was varied from 1-8×10^{-7} Torr BEP which corresponded to 0.3 – 1.1 μm/hr ($3.7 - 13 \times 10^{14}$ atom/cm^{2}s) InN equivalent growth rate. $In_xGa_{1-x}N$ growth temperatures investigated for Series 1 were 550 °C and 600 °C. Seven samples were grown at 550 °C and seven were grown at 600 °C.

The second grown series (Series 2) was grown with an increased Φ_{N*}-Φ_{Ga} deficit to determine how much In incorporation could be achieved at 650 °C and 700 °C. Table 1 lists the fluxes used for the samples in Series 2. To achieve Φ_{N*} = 2.6 μm/hr (3.2×10^{15} atom/cm^{2}s) for samples A and B, a N_2 flow of 10 sccm and a plasma forward power of 500 W were used. To achieve 3.5 μm/hr N* flow (4.3×10^{15} atom/cm^{2}s), the N_2 flow rate was 15 sccm, and a plasma forward power of 500 W was used. Due to the higher growth temperature used for Series 2, the $In_xGa_{1-x}N$ was capped with a thin (5 nm) GaN layer to prevent $In_xGa_{1-x}N$ decomposition during cooling. To grow the cap layer a second Ga cell with a flux larger than Φ_{N*} was opened while the Ga cell used for $In_xGa_{1-x}N$ growth was closed. The In cell was left open. Using $\Phi_{Ga} > \Phi_{N*}$ should prevent any In from incorporating into the cap layer.

At the end of growth for all samples, all cells were shuttered at the same time and the metal adlayer was desorbed as indicated by the RHEED intensity. Once the cells were shuttered, the intensity of the RHEED pattern first increased and then reached a constant steady state value consistent with a fully desorbed adlayer. Then the samples were cooled quickly to prevent $In_xGa_{1-x}N$ decomposition. The RHEED pattern of the final $In_xGa_{1-x}N$ films ranged from spotty

(indicating a 3D surface) for the low Φ_{In} films to streaky (indicating a 2D surface) for the higher Φ_{In} films.

For each $In_xGa_{1-x}N$ film high resolution x-ray diffraction (HRXRD) ω-2θ scans of the (0002) reflection were recorded using a Philips Panalytical MRD Pro system with CuKα_1 radiation with a 4-bounce Ge (220) monochromator and 2-bounce Ge (220) analyzer. Reciprocal space maps (RSMs) of the $(10\bar{1}5)$ reflection were collected using a PIXcel^{3D} detector to confirm that the $In_xGa_{1-x}N$ films were fully coherent with the GaN substrate. $In_xGa_{1-x}N$ film thickness was determined by the spacing of the fringes of the ω-2θ (0002) scan.

The peak separation between the GaN and $In_xGa_{1-x}N$ (0002) peaks was used to determine the $In_xGa_{1-x}N$ alloy composition. Reference values used for the relaxed lattice parameters for pure GaN were a_0 = 3.1896 Å and c_0 = 5.1855 Å [45]. Reference values used for the relaxed lattice parameters for InN were a_0=3.5378 Å and c_0=5.7033 Å [46]. Reference values used for the elastic stiffness tensor elements C_{13} and C_{33} for pure wurtzite GaN and InN were taken from Ref [47]. The wavelength for the CuKα_1 radiation was 1.5406 Å. The procedure to determine the $In_xGa_{1-x}N$ composition is as follows and is based on the assumption that the $In_xGa_{1-x}N$ film is fully coherent to the GaN substrate. First the measured GaN- $In_xGa_{1-x}N$ peak separation and the GaN relaxed reference c_0 lattice parameter were substituted into Bragg's law to determine the measured c lattice spacing of the $In_xGa_{1-x}N$ film. Then a starting guess for alloy composition was chosen. Vegard's law was used to determine the relaxed c and a lattice spacings for $In_xGa_{1-x}N$ as a function of composition from pure GaN and pure InN. Vegard's law was also used to determine the values of C_{13} and C_{33} for $In_xGa_{1-x}N$ as a function of composition based on the values for pure GaN and InN. Then the relaxed $In_xGa_{1-x}N$ a lattice parameter was used to calculate the in-plane ($\varepsilon_{\|}$) via $\epsilon_{\|} = \frac{a_{InGaN}}{a_{InGaN,relaxed}} - 1$. The measured a lattice spacing of the film is known since all

$In_xGa_{1-x}N$ films grown were fully strained to the GaN substrate. The relationship between $\varepsilon_{\parallel}$ and the out-of-plane strain ($\varepsilon_{\perp}$) is $\epsilon_{\perp} = -2\frac{C_{13}}{C_{33}}\epsilon_{\parallel}$. The c lattice parameter calculated from $\varepsilon_{\perp}$ is $c_{InGaN} = c_{InGaN,measured} - \left(c_{0,GaN} \times \epsilon_{\perp}\right)$. This c lattice parameter is then compared to the value obtained from Vegard's law. If the two values do not match, a new guess composition was chosen. This iterative process is performed by MATLAB until the two values match. See Appendix B for the MABLAB code used to do this calculation.

The ω-2θ (0002) scans were also used to determine whether In droplets were present on the surface of the $In_xGa_{1-x}N$ films. It has been documented that an In metal body-centered tetragonal (101) peak exists at an ω value approximately 0.8° less than that of the GaN (0002) substrate peak [48,49].

The surface morphology of each film was characterized via atomic force microscopy (AFM) using an Asylum MFP-3D tool used in the tapping mode in air. Scans were taken at 20×20, 5×5, and 1×1 μm. Root mean squared (RMS) roughness values are reported for 5×5 μm scans.

Sample C of Series 2 was also characterized via atom probe tomography (APT) to determine the alloy composition of the film [50]. The sample was cleaved, and a 150 nm sacrificial GaN capping layer was grown at 720 °C under standard Ga-rich conditions sample to facilitate the preparation of the APT sharp tip. A FEI Helios 600 dual beam FIB instrument was used for the preparation of the specimen [51]. APT experiments were performed with a Cameca 3000X HR Local Electrode Atom Probe (LEAP) operated in laser-pulse mode (13 ps pulse, 532 nm green laser, 10 μm laser spot size) with a sample-based temperature of 45 K. The laser pulse energy and the detection rate for the experiments were respectively set to 0.5 nJ and 0.02 atoms per

pulse. The 3D reconstruction were carried out using a geometrical based algorithm [52] implemented in the commercial software IVAS™ .

4.3 Results

4.3.1 Series 1

Figure 38 (a) and (b) show representative RSM and ω-2θ scans of a sample from Series 1 of composition $In_{0.15}Ga_{0.85}N$ grown at 600 °C. Since all films were fully coherent, the $In_xGa_{1-x}N$ composition was determined from (0002) ω-2θ scans. Not all films had well-defined thickness fringes to accurately determine the $In_xGa_{1-x}N$ thickness. However, among the samples that did have assessable thickness fringes, the $In_xGa_{1-x}N$ growth rates were consistently around 1.2 μm/hr, with the highest growth rate measured of 1.3 μm/hr. No identifiable trend was observed in the growth rate as Φ_{In} was increased.

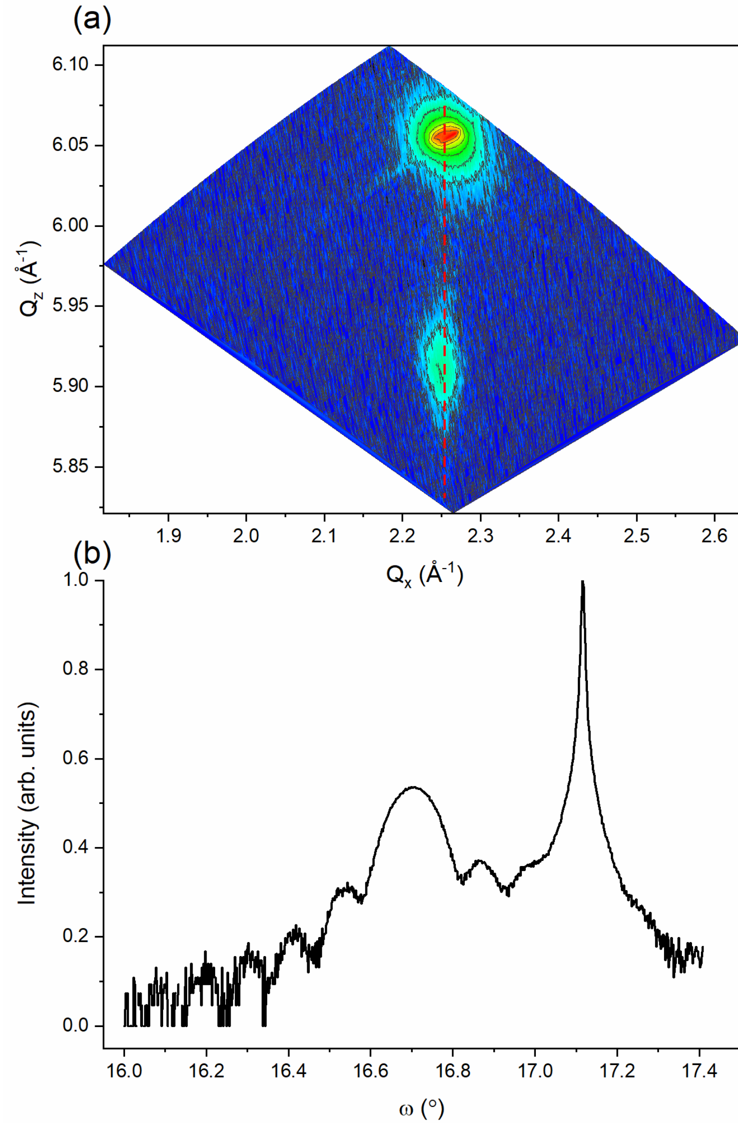

Figure 38 (a) RSM of the $(10\bar{1}5)$ peak of a representative sample from Series 1 of composition $In_{0.15}Ga_{0.85}$ grown at 600 °C. The vertical dashed line is a guide to the eye showing that the film is coherent to the GaN substrate. Fig 2(b) HRXRD ω-2θ triple axis scan of the (0002) peak of the same sample in 2(a). The peak separation between the GaN substrate peak and $In_xGa_{1-x}N$ alloy peak was used to calculate the alloy composition for all samples. The spacing between the smaller fringes was used to calculate the $In_xGa_{1-x}N$ thickness and growth rate.

Figure 39 shows the dependence of composition on Φ_{In} for all 14 samples of Series 1. As expected, alloy composition increases linearly with Φ_{In} until a saturated In wetting layer was realized. Once a saturated In wetting layer had formed, the film composition no longer changed

with increasing Φ_{In}. Films grown in the saturated In wetting layer regime all showed an In metal (101) peak in the ω-2θ (0002) scan, indicating that a saturated wetting layer was reached for both growth temperatures. The Φ_{In} required to reach a saturated wetting layer was 1.07 μm/hr (1.31×10^{15} atom/cm^{2}s) for a growth temperature of 550 °C and 1.44 μm/hr (1.31×10^{15} atom/cm^{2}s) for a growth temperature of 600 °C. The dashed line in Figure 39 indicates the transition from N-rich growth to group III-rich growth. Due to desorption of In from the surface of the sample the Φ_{In} required to achieve a saturated In wetting layer is greater than that required to push the growth into the metal-rich regime. HRXRD ω-2θ (0002) scans of all seven samples grown at 600 °C is shown in Figure 40. The In droplet (101) peak is visible for the two scans with highest Φ_{In}. The saturated In composition was x = 0.25 for samples grown at 550 °C and x = 0.21 for samples grown at 600 °C.

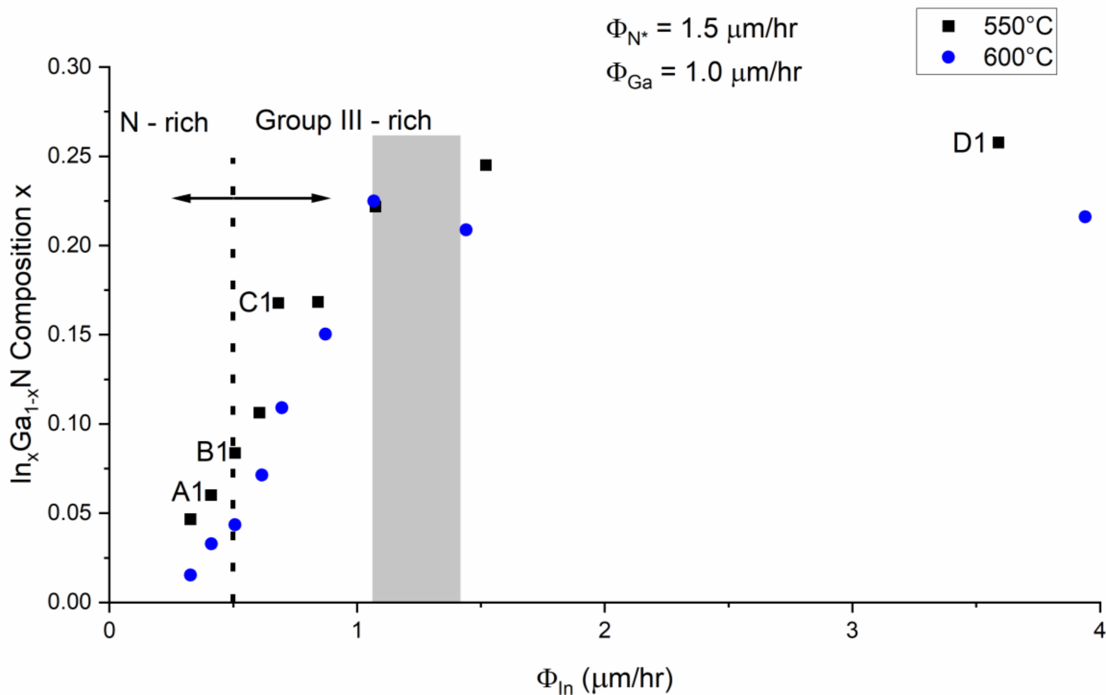

Figure 39 $In_xGa_{1-x}N$ film composition *x* of Series 1 as a function of Φ_{In} and growth temperature. Alloy compositions increases linearly with Φ_{In} for each growth temperature until a saturated In

wetting layer is reached. The gray region represents when the In wetting layer becomes saturated. The dashed line indicates the transition from N-rich growth to group III-rich growth.

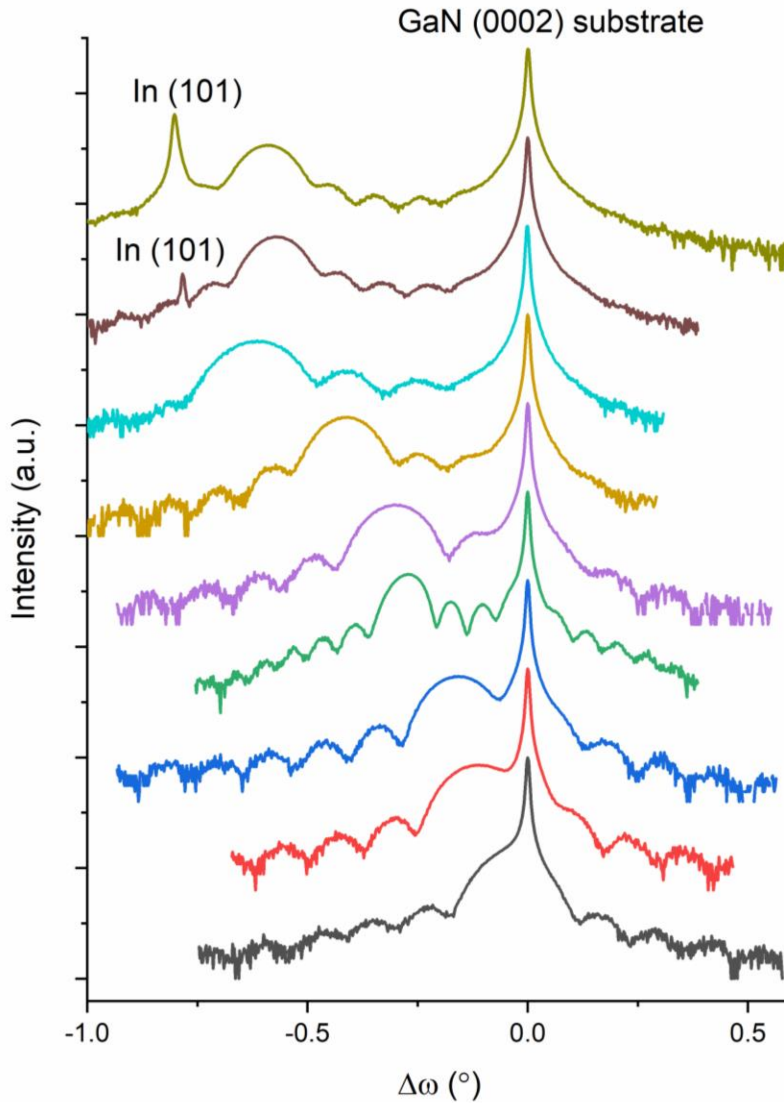

Figure 40 HRXRD ω-2θ scans of all samples in Series 1 grown at 600°C. Δω refers to the distance in degrees from the GaN (0002) substrate peak. The $In_xGa_{1-x}N$ alloy peaks are at a smaller ω than the GaN substrate peak.

Four representative samples (A1, B1, C1, and D1) from Series 1 are identified on Figure 39. AFM scans of these samples are shown in Figure 41. Samples A1 and B1 show mound-type structures forming around threading dislocations, which is similar to the spiral hillock formation

reported in other studies of $In_xGa_{1-x}N$ grown by PAMBE [16]. Samples C1 and D1 do not have clear mound structures. AFM scans are shown on these samples because their morphologies are representative of the other samples in Series 1. The RMS roughness values calculated for samples A1, B1, C1, and D1 are 1.05 nm, 0.93 nm, 1.04 nm, and 1.79 nm, respectively.

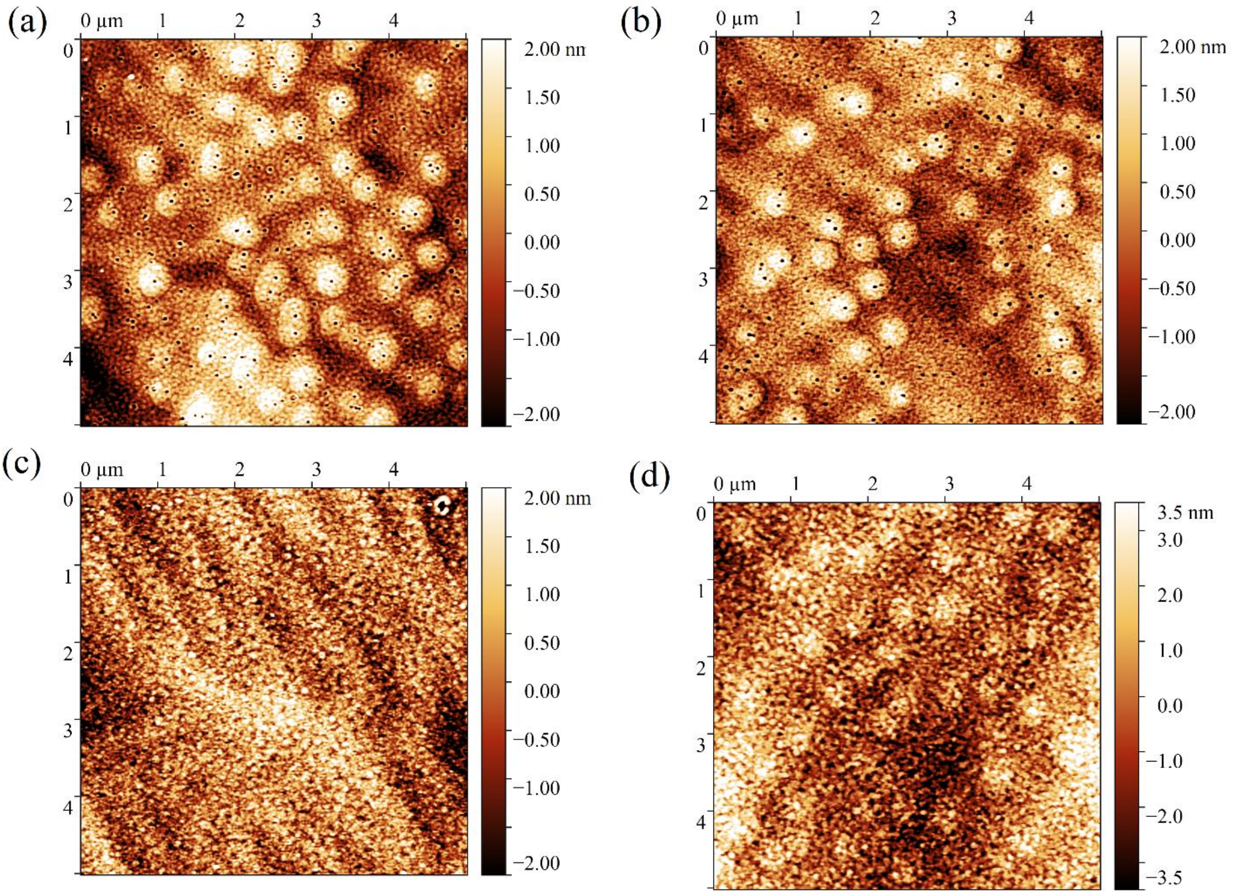

Figure 41 5 × 5 µm AFM scans from samples (a) A1, (b) B1, (c) C1, and (d) D1 in Series 1. RMS roughness values are 1.05 nm, 0.93 nm, 1.04 nm, and 1.79 nm, respectively.

4.3.2 Series 2

Once the high Φ_{N*} $In_xGa_{1-x}N$ growth was established at lower temperatures in Series 1, higher Φ_{N*} was used to determine how hot $In_xGa_{1-x}N$ could be grown with sufficient In incorporation. Table 1Table 2 shows the alloy compositions achieved for samples grown at 650

°C and 700 °C. The alloy composition for samples A2 and B2 were determined via HRXRD in the same way as samples in Series 1. At a growth temperature of 650 °C an alloy composition of $x = 0.148$ was achieved for sample A2 with $\Phi_{In} = 1.89$ µm/hr (2.31×10^{15} atom/cm^{2}s) and $x = 0.177$ was achieved for sample B2 with $\Phi_{In} = 3.17$ µm/hr (3.87×10^{15} atom/cm^{2}s). A saturated In wetting layer was not observed for any of the samples in Series 2. AFM scans for samples A2 and B2 show a mound morphology similar to samples A1 and B1 in Series 1 and have RMS roughness values of 1.40 nm and 1.61 nm respectively.

Table 2. Growth details for Series 2. Fluxes are noted in terms of GaN equivalent growth rates for Ga and N*, InN equivalent growth rates for In, as well as atomic fluxes.

Sample	Growth Temperature (°C)	Φ_{In} (µm/hr) (*atom/cm²s*)	Φ_{N*} (µm/hr) (*atom/cm²s*)	Φ_{N*}-Φ_{Ga} (µm/hr) (*atom/cm²s*)	$In_xGa_{1-x}N$ Composition x	$In_xGa_{1-x}N$ Growth Rate (µm/hr)
A2	650	1.89 *2.31×10^{15}*	2.6 *3.2×10^{15}*	2.50 *3.05×10^{15}*	0.148[a]	0.14[a]
B2	650	3.17 *3.87×10^{15}*	2.6 *3.2×10^{15}*	2.50 *3.05×10^{15}*	0.177[a]	0.15[a]
C2	700	3.70 *4.52×10^{15}*	3.5 *4.3×10^{15}*	1.57 *1.92×10^{15}*	0.05[b]	0.06[b]

Determination of the film composition for sample C2 grown at 700 °C was not possible via HRXRD. The ω-2θ (0002) scan for sample C2 (shown in Figure 42) did not have a separate alloy peak. Thickness fringes are visible, but it is unclear if they are from the GaN cap layer or an $In_xGa_{1-x}N$ layer. The APT 3D reconstruction of sample C2 shown in Figure 43(a) and the corresponding In 1D concentration profile along the growth direction in Figure 43(b) indicates an $In_xGa_{1-x}N$ composition of $x = 0.05$. The film thickness was less than 10 nm, resulting in a growth rate of only 1-2 nm/min.

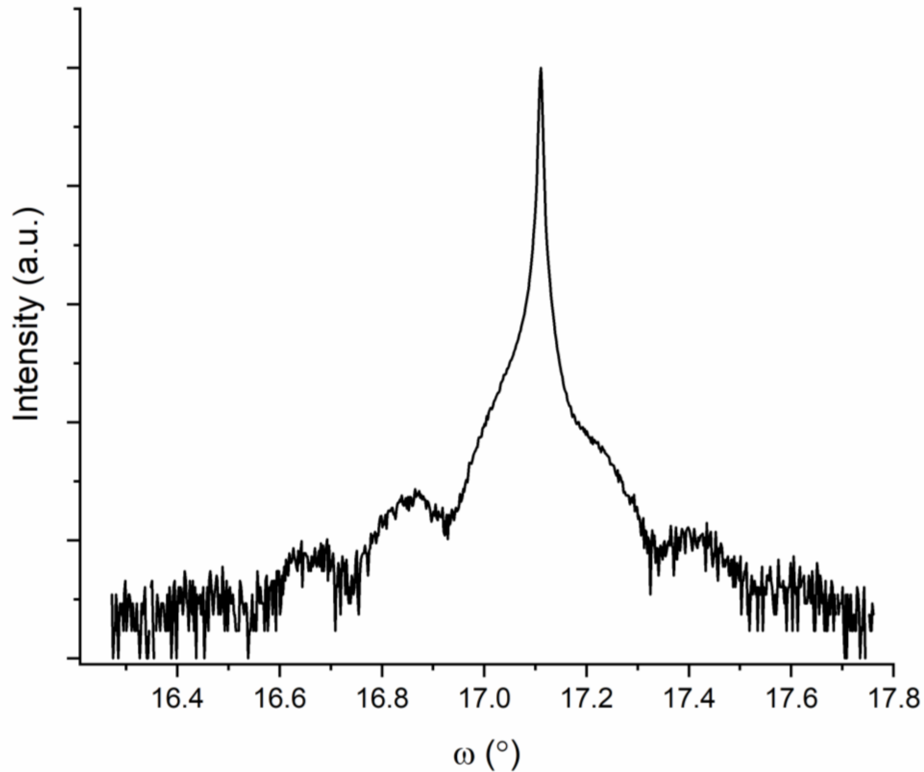

Figure 42. HRXRD ω-2θ scan of sample C2 from Series 2 showing thickness fringes, but no separate $In_xGa_{1-x}N$ alloy peak.

In the 1D concentration profile in Figure 43(b) Sample C2 also shows around x = 0.005 In incorporation in the GaN cap layer. Since the In source shutter was open during the GaN cap growth, it is possible that the In incorporated as the film was grown even though Φ_{Ga} was greater than Φ_{N*}, which should prevent any In incorporation.

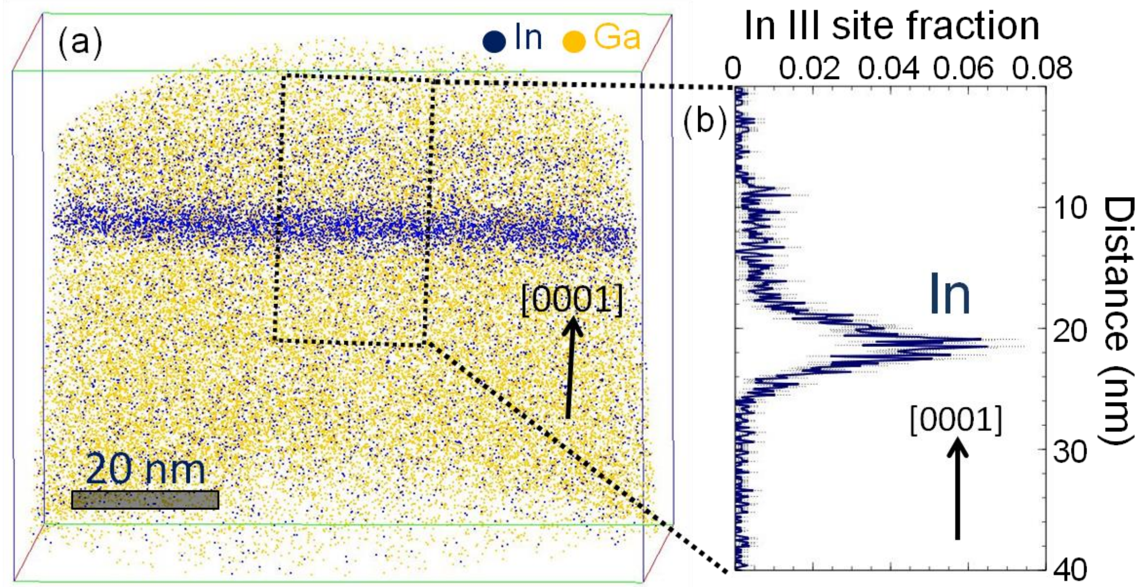

Figure 43 (a) APT 3D reconstruction of sample C2 in Series 2 shown an $In_xGa_{1-x}N$ layer is present. (b) 1D concentration profile measured from the center of the 3D reconstruction and along the growth direction showing the amount of In incorporated in the layer. APT data courtesy Dr. Bastien Bonef.

The 5×5 μm AFM scan of sample C2 is shown in Figure 44. This sample does not show mound morphology, but rather step-terrace morphology and has an RMS roughness of 0.70 nm. It is important to note that the morphology could be in part attributed to the thin (5 nm) GaN cap rather than the underlying $In_xGa_{1-x}N$.

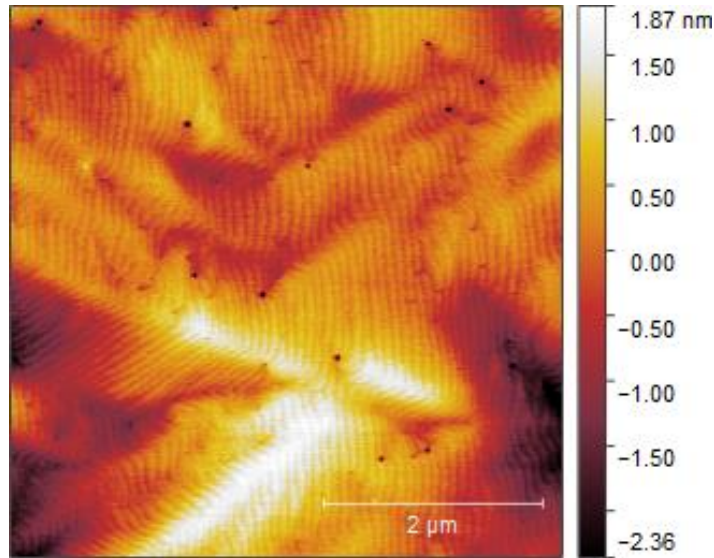

Figure 44. AFM scan of sample C2 from Series 2 showing step-terrace surface morphology and an RMS surface roughness of 0.70 nm.

4.4 Discussion

As shown in Figure 39, once a saturated In wetting layer is reached, the film composition no longer changes with increasing Φ_{In}. This is the first confirmation that PAMBE $In_xGa_{1-x}N$ growth at high growth rates follows the same trend with increasing Φ_{In} as observed at the more common growth rates around 200 – 300 nm/hr [48,49]. Hestroffer et al. [49] reported a saturated In composition of x = 0.18 for a growth temperature of 575 °C and Gacevic et al. [48] reported In compositions ranging from x = 0 to x = 0.50 depending on growth temperature and incident Φ_{In}.

Even though there is no thermodynamic equilibrium during MBE growth (since it is impossible to define a temperature for the molecular beam), the saturation of the In content in the films can be understood as the chemical potential of In in the film ($\mu_{In,\ film}$) being equal to the chemical potential of liquid In in the droplets and wetting layer ($\mu_{In,\ drop}$). So $\mu_{In,\ wetting\ layer} = \mu_{In,\ droplet} = \mu_{In,\ film}$. The In droplets act as an In reservoir that “feeds” the adlayer. A schematic representing the In exchange is shown in Figure 45.

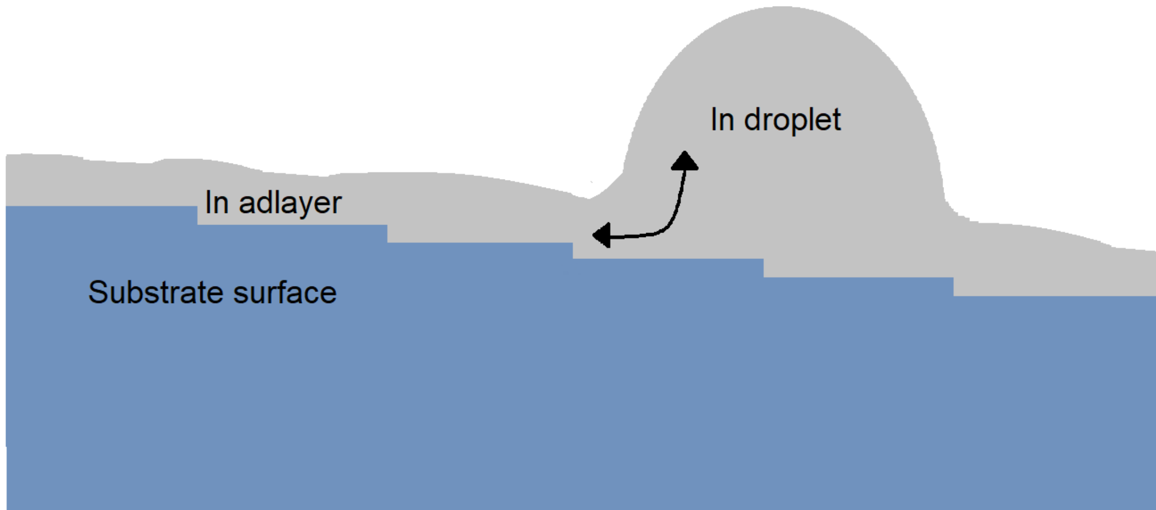

Figure 45. Schematic showing In exchange between the droplets and In adlayer present on the growing film.

It is also clear that there is a large desorbing Φ_{In} from the sample surface during $In_xGa_{1-x}N$ growth from desorption of In from the adlayer. Note in these studies $\Phi_{In} + \Phi_{Ga} > \Phi_{N^*}$ for most samples and thus we expect at steady state there must be significant In desorption as Ga should preferentially incorporate over In in the growing $In_xGa_{1-x}N$ film for metal-rich growth. A comparison of the vapor pressure of liquid In and Ga at relevant growth temperatures illustrates this desorbing Φ_{In}. At a growth temperature of 600 °C, $p_{In, liq} = 1.6 \times 10^{-6}$ Torr and $p_{Ga, liq} = 4.1 \times 10^{-8}$ Torr [53]. Almost two orders of magnitude difference in vapor pressure results in a film that has a much lower In content than would be expected based on the ratio of Φ_{In}/Φ_{Ga} alone. This $p_{In, liq}$ is approximately equal to the BEP of In. At the even higher growth temperatures explored in Series 2 (650 °C and 700 °C), the difference in vapor pressures between the two group III elements is even larger. At 700 °C there is 3 orders of magnitude difference between $p_{In, liq}$ and $p_{Ga, liq}$. Once the In wetting layer is saturated, the equilibrium desorbing In flux is equal to the vapor pressure of In, $\Phi_{In, desorb} = \Phi_{In, liq}$.

This large desorbing Φ_{In} becomes more extreme as growth temperature increases. At 700 °C the net $In_xGa_{1-x}N$ growth rate is so low that the film is barely growing faster than it is decomposing. For growth temperatures of 650 °C and below, the growth rate is governed mainly by Φ_{Ga} forming Ga-N bonds, with a small component being added from the In that actually participates in bonding. For sample C2 the growth rate does not follow Φ_{Ga} = 1.03 μm/hr, which suggests Ga-N bonds are also decomposing.

For growth with a saturated In wetting layer, the film composition is determined by the growth temperature and the Φ_{N*} - Φ_{Ga} deficit. It seems that growth temperature has a larger effect than the absolute Φ_{N*}, although this work does not include samples grown at the more common Φ_{N*} 0.2 – 0.3 μm/hr for comparison. The formation of the saturated In wetting layer represents the maximum chemical potential for in ($\mu_{In,\,max}$) for a given growth temperature and Φ_{N*} - Φ_{Ga} deficit. Thus the maximum In incorporation under a saturated In wetting layer represents the solubility limit of In in $In_xGa_{1-x}N$ for that growth temperature and Φ_{N*}-Φ_{Ga} deficit.

In Ref. [49], which reports a maximum growth rate of 265 nm/hr under a saturated In wetting layer, the growth rate is shown to increase linearly from 200 nm/hr to 260 nm/hr with increasing Φ_{In} just like film composition. This is not observed for high growth rate $In_xGa_{1-x}N$ in this work. This is because the overall growth rate is so high that the small incremental change provided by slightly more In incorporation is not large enough to be more than noise.

Samples A1, B1, A2, and B2 all exhibit mound morphology. But as Φ_{In} increases and the growth temperature increases, samples exhibit planar morphology, with atomic steps visible on sample C2 but not on samples C1 and D1. This indicates that as the In adlayer develops and the growth temperature increases, surface adatom mobility is enhanced, thus eliminating the mound structures.

Since the motivation for growing $In_xGa_{1-x}N$ at high active nitrogen fluxes was derived in part from extrapolating the modeling by Turski et al. [41], it is important to see if the present work follows the trends seen in that work conducted at lower growth rates. Previous models for PAMBE growth of $In_xGa_{1-x}N$ expressed the desorbing nitrogen flux $(\Phi_N^{\nearrow})$ due to In-N bond decomposition as $\Phi_N^{\nearrow} = C \cdot x \cdot exp\left(-\frac{E_a(x)}{kT}\right)$ where C is a constant, x is the film composition, E_a is an energy barrier that depends on film composition x, and T is the growth temperature [54]. In Ref. [41] however, the authors point out that on a vicinal GaN surface there are two types of c/2 atomic steps (A and B) that differ in the number of bonds a N atom landing on the surface can satisfy. Based on these "non-equivalent" atomic steps they express the desorbing nitrogen flux as $\Phi_N^{\nearrow} = \left(\frac{C_A}{\Phi_N^{\searrow}} + \frac{C_B}{\Phi_{Ga}^{\searrow}}\right) \cdot (\Phi_N^{\searrow} - \Phi_{Ga}^{\searrow}) \cdot exp\left(-\frac{E_a(x)}{kT}\right)$ where C_A and C_B are constants associated with atomic steps A and B, respectively and $\Phi_N^{\searrow}$ and $\Phi_{Ga}^{\searrow}$ are the incident N and Ga fluxes, respectively. Then the study goes on to grow a series of $In_xGa_{1-x}N$ films at a variety of different Φ_{N*}, Φ_{Ga}, and growth temperatures to fit the constants C_A and C_B. It is important to note that in Ref. [41] the authors state that all samples were grown under a saturated In wetting layer.

If the nonequivalent atomic step model presented in Ref. [41] is extrapolated to the growth rates in Series 1 of this work, the maximum In incorporation at a growth temperature of 550 °C and 600 °C is predicted to be 32.4% and 28.4%, respectively. This is higher than the observed maximum In incorporation of 25.8% and 22.5%. This could be due to differences in growth temperature between different MBE systems (since optical pyrometry is only a precise, but not necessarily accurate technique). Since the maximum Φ_{N*} used by Turski et. al [41] is 0.55 µm/hr (6.72×10^{15} atom/cm^{2}s), it could also be the case that extrapolating to Φ_{N*} = 1.0 µm/hr (1.2×10^{15} atom/cm^{2}s) is beyond the limits of the model's accuracy. It is important to note that since

the modeling assumes the presence of a saturated In wetting layer, it is not appropriate to apply the model to Series 2, where all samples are grown before the onset of a saturated In wetting layer.

Since impurity incorporation in growing films is inversely proportional to the growth rate, growing $In_xGa_{1-x}N$ films at these elevated growth rates could greatly improve the material quality and could lead to more efficient PAMBE III-N LEDs. One important consideration in the growth of $In_xGa_{1-x}N$ GaN active regions is having precise control over the thickness of quantum wells. Growth rates that are too high could lead to a loss of control over film thickness if the growth time approaches the MBE shutter rise and fall times. Even at the highest growth rate reported in this work (1.3 μm/hr), a 3 nm quantum well corresponds to a 8.4 s growth time, which is sufficiently longer than the approximately 5 ms shutter rise and fall time. Elevated growth rates could also be useful for growing thick, relaxed $In_xGa_{1-x}N$ layers for applications where strain reduction of higher In composition layers is desirable.

Future work is currently planned to determine the maximum possible In content in $In_xGa_{1-x}N$ films at 700 °C. While it may be possible through optimization of growth conditions to reach film compositions useful for blue emitting optoelectronic devices, it seems unlikely that higher compositions corresponding to longer wavelength devices is possible at such high growth temperatures.

Growth at these elevated atomic fluxes comes with logistical challenges, however. Several modifications have been made to the MBE system in this study over the years that this high flux plasma unit has been in use. When group III effusion cells are operated at high capacity for an extended length of time, source material can be depleted rapidly. Over the history of high-flux research at our university, both Ga effusion cells and the In effusion cell have been replaced with

higher capacity cells to reduce downtime related to source material refilling. With N_2 gas flows as high as 15 sccm, extra pumping has been added to the system to keep the pressure during growth at an acceptable level. During high flux growth, it is typical for the growth chamber pressure to reach the mid 10^{-5} Torr range. Parts inside the chamber can become coated in III-N material quickly, requiring more frequent replacement and cleaning of parts like mounting blocks, RHEED screens, and viewports. The extra cost associated with these issues may prove to be unrealistic for some groups.

Another technical consideration is that the high-flux plasma unit is currently not capable of growing at the more traditional lower growth rates (around 300 nm/hr) on which earlier work from our group was based. Instead of replacing the older plasma unit, we have opted to keep both the lower-flux and higher-flux units on the system. This uses an extra source port that some MBE systems might not have to spare. As more work on the possibilities of high-flux PAMBE III-N growth is done, groups will have to weigh the benefits and costs of this new technique.

4.5 Conclusions

In this work we investigated the effect of high active nitrogen flux on the incorporation of In into $In_xGa_{1-x}N$ films at low and elevated growth temperatures. Using a high Φ_{N*} at lower PAMBE $In_xGa_{1-x}N$ growth temperatures resulted in $In_xGa_{1-x}N$ growth rates of up to 1.3 μm/hr and mound-like surface morphology. In incorporation follows linearly with Φ_{In} before the onset of a saturated In wetting layer, just as for lower growth rate $In_xGa_{1-x}N$ reported in the literature.

We have also shown that In incorporation into $In_xGa_{1-x}N$ films is possible at 700 °C, which has not been demonstrated previously in the literature. The film grown at 700 °C shows very smooth step-terrace surface morphology and no spiral hillocks. It is expected that increasing Φ_{N*} further will result in more In incorporation. It is important to note that at 700 °C the $In_xGa_{1-x}N$

growth rate is only a few nm/min even though the constituent fluxes are all over 1.0 μm/hr (1.2×10^{15} atom/cm^{2}s). This is because the film is decomposing so quickly that the net growth rate is extremely slow.

Further optimization of $In_xGa_{1-x}N$ at 700 °C is planned to maximize In incorporation into the film. Optical characterization of $In_xGa_{1-x}N$ films grown with high Φ_{N^*} is also planned as well as eventual integration into all PAMBE LEDs. This work represents a viable path forward to achieving efficient III-N PAMBE LEDs.

References

[1] Y. Taniyasu, M. Kasu, and T. Makimoto, Nature **441**, 325 (2006).
[2] C.S. Gallinat, G. Koblmüller, J.S. Brown, S. Bernardis, J.S. Speck, G.D. Chern, E.D. Readinger, H. Shen, and M. Wraback, Appl. Phys. Lett. **89**, 032109 (2006).
[3] L.Y. Kuritzky and J.S. Speck, MRS Commun **5**, 463 (2015).
[4] R. Quay, *Gallium Nitride Electronics* (Springer Science & Business Media, 2008).
[5] C. Weisbuch, M. Piccardo, L. Martinelli, J. Iveland, J. Peretti, and J.S. Speck, Phys. Status Solidi A **212**, 899 (2015).
[6] J. Orton and T. Foxon, *Molecular Beam Epitaxy: A Short History* (Oxford University Press, 2015).
[7] G. Koblmüller, R. Averbeck, H. Riechert, and P. Pongratz, Phys. Rev. B **69**, 035325 (2004).
[8] J. Neugebauer, T.K. Zywietz, M. Scheffler, J.E. Northrup, H. Chen, and R.M. Feenstra, Phys. Rev. Lett. **90**, 056101 (2003).
[9] G. Koblmüller, J. Brown, R. Averbeck, H. Riechert, P. Pongratz, and J.S. Speck, Appl. Phys. Lett. **86**, 041908 (2005).
[10] B.M. McSkimming, C. Chaix, and J.S. Speck, Journal of Vacuum Science & Technology A: Vacuum, Surfaces, and Films **33**, 05E128 (2015).
[11] J. Osaka, M. Senthil Kumar, H. Toyoda, T. Ishijima, H. Sugai, and T. Mizutani, Appl. Phys. Lett. **90**, 172114 (2007).
[12] K. Klosek, M. Sobanska, G. Tchutchulashvili, Z.R. Zytkiewicz, H. Teisseyre, and L. Klopotowski, Thin Solid Films **534**, 107 (2013).
[13] E. Iliopoulos, A. Adikimenakis, E. Dimakis, K. Tsagaraki, G. Konstantinidis, and A. Georgakilas, Journal of Crystal Growth **278**, 426 (2005).
[14] B.M. McSkimming, F. Wu, T. Huault, C. Chaix, and J.S. Speck, Journal of Crystal Growth **386**, 168 (2014).
[15] G. Koblmüller, F. Wu, T. Mates, J.S. Speck, S. Fernández-Garrido, and E. Calleja, Appl. Phys. Lett. **91**, 221905 (2007).
[16] K. Hestroffer, C. Lund, H. Li, S. Keller, J.S. Speck, and U.K. Mishra, Phys. Stat. Sol. (b) **253**, 626 (2016).
[17] C.S. Gallinat, G. Koblmuller, J.S. Brown, and J.S. Speck, J Appl Phys **102**, 064907 (2007).
[18] A.C. Espenlaub, D.J. Myers, E.C. Young, S. Marcinkevičius, C. Weisbuch, and J.S. Speck, J Appl Phys **126**, 184502 (2019).
[19] D.J. Myers, A.C. Espenlaub, K. Gelzinyte, E.C. Young, L. Martinelli, J. Peretti, C. Weisbuch, and J.S. Speck, Appl. Phys. Lett. **116**, 091102 (2020).
[20] J.-X. Shen, D. Wickramaratne, C.E. Dreyer, A. Alkauskas, E. Young, J.S. Speck, and C.G.V. de Walle, Appl. Phys. Express **10**, 021001 (2017).
[21] B.P. Yonkee, E.C. Young, S.P. DenBaars, S. Nakamura, and J.S. Speck, Appl. Phys. Lett. **109**, 191104 (2016).
[22] ARPA-E, (2016).
[23] Y. Zhang, (2020).
[24] E.C. Young, N. Grandjean, T.E. Mates, and J.S. Speck, Appl. Phys. Lett. **109**, 212103 (2016).
[25] L. Mouche, F. Tardif, and J. Derrien, J. Electrochem. Soc. **142**, 2395 (1995).
[26] A.J. Ptak, D.J. Friedman, S. Kurtz, R.C. Reedy, M. Young, D.B. Jackrel, H.B. Yuen, S.R. Bank, M.A. Wistey, and J.S. Harris, J. Vac. Sci. Technol., B **24**, 1540 (2006).

[27] D.F. Storm, M.T. Hardy, D.S. Katzer, N. Nepal, B.P. Downey, D.J. Meyer, T.O. McConkie, L. Zhou, and D.J. Smith, Journal of Crystal Growth **456**, 121 (2016).
[28] D.F. Storm, T. McConkie, D.S. Katzer, B.P. Downey, M.T. Hardy, D.J. Meyer, and D.J. Smith, Journal of Crystal Growth **409**, 14 (2015).
[29] D.F. Storm, T.O. McConkie, M.T. Hardy, D.S. Katzer, N. Nepal, D.J. Meyer, and D.J. Smith, J Vac Sci Technol B **35**, 02B109 (2017).
[30] C.A. Robertson Bayless, Defect-Mediated Carrier Transport Mechanisms in Vertical GaN p-n Diodes, Ph.D., University of California, Santa Barbara, 2019.
[31] C. Wurm, E. Ahmadi, F. Wu, N. Hatui, S. Keller, J. Speck, and U. Mishra, Solid State Communications **305**, 113763 (2020).
[32] G. Koblmüller, R.M. Chu, A. Raman, U.K. Mishra, and J.S. Speck, J Appl Phys **107**, 043527 (2010).
[33] H. Nagayoshi, M. Yamaguchi, K. Kamisako, T. Horigome, and Y. Tarui, Jpn. J. Appl. Phys. **33**, L621 (1994).
[34] S.P. Kowalczyk, D.L. Miller, J.R. Waldrop, P.G. Newman, and R.W. Grant, Journal of Vacuum Science and Technology **19**, 255 (1981).
[35] Y. Enatsu, C. Gupta, S. Keller, S. Nakamura, and U.K. Mishra, Semicond. Sci. Technol. **32**, 105013 (2017).
[36] Y. Chang and H. Kroemer, Appl. Phys. Lett. **45**, 449 (1984).
[37] S. Fernandez-Garrido, G. Koblmuller, E. Calleja, and J.S. Speck, J Appl Phys **104**, 033541 (2008).
[38] M.J. Grundmann and U.K. Mishra, Phys. Status Solidi (c) **4**, 2830 (2007).
[39] C. Skierbiszewski, Z.R. Wasilewski, I. Grzegory, and S. Porowski, J Cryst Growth **311**, 1632 (2009).
[40] P. Waltereit, H. Sato, C. Poblenz, D.S. Green, J.S. Brown, M. McLaurin, T. Katona, S.P. DenBaars, J.S. Speck, J.-H. Liang, M. Kato, H. Tamura, S. Omori, and C. Funaoka, Appl. Phys. Lett. **84**, 2748 (2004).
[41] H. Turski, M. Siekacz, Z.R. Wasilewski, M. Sawicka, S. Porowski, and C. Skierbiszewski, J Cryst Growth **367**, 115 (2013).
[42] M. Siekacz, A. Feduniewicz-Żmuda, G. Cywiński, M. Kryśko, I. Grzegory, S. Krukowski, K.E. Waldrip, W. Jantsch, Z.R. Wasilewski, S. Porowski, and C. Skierbiszewski, J Cryst Growth **310**, 3983 (2008).
[43] H. Turski, M. Siekacz, M. Sawicka, Z.R. Wasilewski, S. Porowski, and C. Skierbiszewski, Jpn. J. Appl. Phys. **52**, 08JE02 (2013).
[44] B.P. Gunning, E.A. Clinton, J.J. Merola, A. Doolittle, and R.C. Bresnahan, Journal of Applied Physics **118**, 155302 (2015).
[45] M. Yamaguchi, T. Yagi, T. Sota, T. Deguchi, K. Shimada, and S. Nakamura, Journal of Applied Physics **85**, 8502 (1999).
[46] W. Paszkowicz, Powder Diffraction **14**, 258 (1999).
[47] A.F. Wright, Journal of Applied Physics **82**, 2833 (1997).
[48] Z. Gacevic, V.J. Gomez, N.G. Lepetit, P.E.D. Soto Rodriguez, A. Bengoechea, S. Fernandez-Garrido, R. Notzel, and E. Calleja, J Cryst Growth **364**, 123 (2013).
[49] K. Hestroffer, F. Wu, H. Li, C. Lund, S. Keller, J.S. Speck, and U.K. Mishra, Semicond. Sci. Technol. **30**, 105015 (2015).
[50] B. Bonef, M. Catalano, C. Lund, S.P. Denbaars, S. Nakamura, U.K. Mishra, M.J. Kim, and S. Keller, Appl. Phys. Lett. **110**, 143101 (2017).

[51] K. Thompson, D. Lawrence, D.J. Larson, J.D. Olson, T.F. Kelly, and B. Gorman, Ultramicroscopy **107**, 131 (2007).
[52] F. Vurpillot, B. Gault, B.P. Geiser, and D.J. Larson, Ultramicroscopy **132**, 19 (2013).
[53] C.B. Alcock, V.P. Itkin, and M.K. Horrigan, Canadian Metallurgical Quarterly **23**, 309 (1984).
[54] R. Averbeck and H. Riechert, Physica Status Solidi (a) **176**, 301 (1999).

Appendix A: Calibration of an optical pyrometer

To calibrate an optical pyrometer, you will need to select an emissivity value that will take the signal from the pyrometer and turn it into an actual temperature. In our lab, we calibrate our pyrometers to the melting point of Al (660 °C). You will need to perform a separate pyrometer calibration for different substrates (GaN on sapphire, free-standing GaN, SiC, etc.), different mounting techniques (metal faceplates with quartz backers vs. In-bonding to a Si wafer), different metals used to coat the backside of your wafers, and for single-side vs double-sided polished wafers. On the PAMBE system, we use 500 nm of Ti on the back of our wafers. The blackbody radiation from the Ti is the signal that the pyrometer is reading. For single-side polished wafers the Ti adheres nicely to the rough backside, but it can flake off for double-side polished wafers. With that being said, I have still been able to use double-side polished wafers with Ti backside coating without too much difficulty. If desired, you can chemically or mechanically roughen the backside to help the Ti adhere.

After you coat the back of your wafers with Ti with an e-beam evaporator, dice or cleave them into your desired size. Then solvent clean with three minutes each in acetone, methanol, and isopropanol in an ultrasonicating bath. Next you will deposit a thin strip of 500 nm thick Al on the epi-side of the wafer with an e-beam evaporator. Our typical sample sizes are 1 × 1 cm or ¼ of a 2” wafer. You will want to orient the Al-strip so that it is off-center on the sample so that you have room to aim the pyrometer. Below is a schematic. You can use either Kapton tape or Al foil to mask the sample in the e-beam. The quality of the Ti and Al films is not as important as it would be for a contact, so you can use higher deposition rates in the e-beam evaporator than you would during device processing.

When you solvent clean the calibration sample before loading into the MBE, do not sonicate it, because this may cause the Al to peel off of the sample. Mount the sample with your desired method and follow your standard out-gassing procedure before loading it into the growth chamber. Setting the emissivity is a two-person job, since one person needs to be aiming the pyrometer and the other needs to adjust the emissivity value on the pyrometer receiver. You will want to have a viewport on the growth chamber with a light shining into it so that you can see the sample clearly. If necessary, rotate the sample so you have the best view of the Al strip. Slowly heat up the sample using manual power control (not the PID). The person aiming the pyrometer is watching for the Al strip to melt. You will see the strip become less shiny when it melts, and it may ball up. Once you see it melt, signal the person adjusting the emissivity to set the value such that the temperature reads 660 °C. Make sure that the pyrometer is being aimed at the part of the sample without the Al strip (like in the schematic). It is important to heat slowly to get an accurate reading.

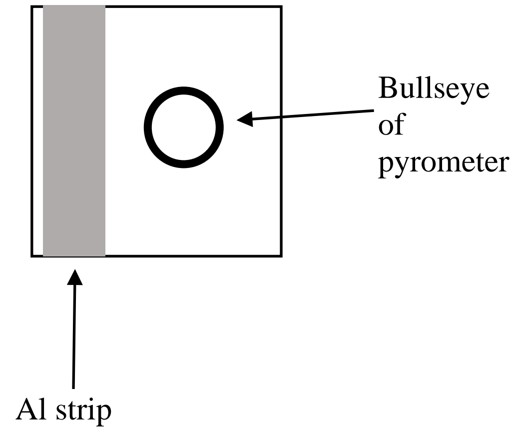

It is important to remember that optical pyrometry used in this way is a precise, but not necessarily accurate technique. Your relative temperature differences will be accurate, but not the absolute temperature value. This is important to keep in mind when referencing literature values of temperature obtained via pyrometry. Temperature readings can vary greatly between different MBE systems. The optimal growth temperature on your MBE may be different than others. Other more accurate methods of temperature measurement exist but are much more expensive than optical pyrometry.

One additional note is for the NH_3-Assisted MBE system. In the past, researchers had issues with the Ti backing metal becoming nitrided with exposure to NH_3, which changed the temperature reading over long growths. To fix this they now use a Ti/Pd/Ti stack that reduces nitridation of the backside metal and results in more stable temperature readings. I have not had an issue with Ti nitridation with plasma growth (even with extremely high nitrogen fluxes). If you do use other backside metal stacks in addition to Ti you will need separate emissivity calibrations for each metal stack used.

Appendix B: MATLAB code for determination of $In_xGa_{1-x}N$ composition

This code calculates the $In_xGa_{1-x}N$ composition *x* for fully strained InGaN on GaN films. The inputs into this code are the ω peak positions of the 0002 GaN substrate peak and InGaN alloy peak that have been fitted separately to a Gaussian.

```
%%Fit GaN & InGaN peak positions to Gaussian and calculate composition
%%from Vegard's Law for fully strained InGaN on GaN

clear

tdfread('080219A_om2th_002.txt');
semilogy(Angle,Intensity)
xlabel('\omega ^{o}')
ylabel('Intensity (arb)')

lambda=1.5405974;%Angstrom, Cu Kapha1
tol=0.001;%tolerance for percent error

x_guess=0.05;%Initial guess for composition

%Elastic constants for pure InN and GaN
C13_GaN=103;%GPa
C33_GaN=405;%GPa
C13_InN=92;%GPa
C33_InN=224;%GPa

%Relaxed lattice parameters of pure InN and GaN
a0_InN=3.5378;%Angstrom
c0_InN=5.7033;%Angstrom
a0_GaN=3.1896;%Angstrom
c0_GaN=5.1855;%Angstrom

d_GaN_002=(1/2)*c0_GaN;%Angstrom
theta_GaN_002_theory=asin(lambda/(2*d_GaN_002))*(180/pi);%degrees

%INPUT
omega_GaN=17.4640;%GaN peak position in degrees, from fitting
omega_InGaN=16.87446;%InGaN peak position in degrees, from fitting
delta_omega=omega_InGaN-omega_GaN;%degrees

d_002_InGaN_meas=lambda/(2*sin((theta_GaN_002_theory+delta_omega)*(pi/180)));
```

```
c_InGaN_meas=2*d_002_InGaN_meas;
a_InGaN_meas=a0_GaN;%for fully-strained film

a_InGaN_relax=(x_guess*a0_InN)+((1-x_guess)*a0_GaN);%InGaN a for x_guess if relaxed
from Vegard
c_InGaN_relax=(x_guess*c0_InN)+((1-x_guess)*c0_GaN);%InGaN c for x_guess if relaxed
from Vegard

C13_inter=x_guess*C13_InN+(1-x_guess)*C13_GaN;%InGaN C13 interpolated for x_guess
C33_inter=x_guess*C33_InN+(1-x_guess)*C33_GaN;%InGaN C33 interpolated for x_guess

epsilon_para=(a_InGaN_meas/a_InGaN_relax)-1;%strain in plane
epsilon_perp=-2*(C13_inter/C33_inter)*epsilon_para;%strain out of plane

c_x_guess=c_InGaN_meas-(c0_GaN*epsilon_perp);%relaxed c_InGaN from strain
c_error=100*(c_x_guess-c_InGaN_relax)/c_InGaN_relax;%percent
count=0;

while abs(c_error) > tol
    if c_error > 0
        x_guess=x_guess+0.0001;
     elseif c_error < 0
        x_guess=x_guess-0.0001;
    end
   count=count+1;
   a_InGaN_relax=x_guess*a0_InN+(1-x_guess)*a0_GaN;
   c_InGaN_relax=x_guess*c0_InN+(1-x_guess)*c0_GaN;

   C13_inter=x_guess*C13_InN+(1-x_guess)*C13_GaN;
   C33_inter=x_guess*C33_InN+(1-x_guess)*C33_GaN;

   epsilon_para=(a_InGaN_meas/a_InGaN_relax)-1;
   epsilon_perp=-2*(C13_inter/C33_inter)*epsilon_para;

   c_x_guess=c_InGaN_meas-(c0_GaN*epsilon_perp);
   c_error=100*(c_x_guess-c_InGaN_relax)/c_InGaN_relax;

end
```